Norwegian University of Science and Technology (NTNU)

Postnatal Development of Parvalbumin-Immunoreactive Cells in the Medial Entorhinal Cortex of the Rat: Morphology, Connectivity and Ultrastructure

Master´s Thesis
Faculty of Medicine

Supervisor: Nina Berggaard

Anna E. Bråthen Paulsen
Trondheim, June 2016

Acknowledgement

This study was carried out at the cellular and molecular image core facility (CMIC) at the Norwegian University of Science and Technology (NTNU), under the supervision of Nina Berggaard. All experiments are done in cooperation with Nina and Ingvild Bjerke.

First of all, I want to express my deepest gratitude to Nina, for the enormous amount of time you have spent helping us, for help during the wright-up of the thesis and for all that you have taught me. A special thank also belong to Ingvild, my dear friend and office snake, for all of the collaboration in the lab, for hours of laughter and for all the good conversations we´ve shared. This would not have been possible without either of you.

I also want to thank Johannes for sharing his knowledge and passion for research and electron microscopy. A huge thanks goes to Nan and Linh for all of their technical assistance, for teaching me the skills needed for this work and for always being happy to answer questions. I would also like to thank Gro and Gunnar for their support in the lab.

As for the people outside the lab, a huge thanks goes to my loving family and friends for cheering me on and support during my studies. I especially want to thank my dad and brother for proofreading my text. Last but not least, a special thanks goes to Thomas, for help during the wright-up of the thesis and for all your support.

Abstract

Grid cells in layer II of the the medial entorhinal cortex (MEC) generate metric spatial representations. Resent research indicates that the grid-cell firing pattern may emerge through recurrent connections with local parvalbumin-containing (PV+) interneurons. Knowledge about the MEC PV+ cells and their connectivity with grid cells have mainly been obtained from electrophysiological studies in the adult MEC, and little is known about the PV+ cells or their connectivity within the MEC at the ultrastructural level. Although the PV+ cells and their connections must be present before the grid firing pattern can emerge, little is known about the PV+ cells or their connections during development.

In this study, maturation of PV+ cells within the rat MEC was examined at postnatal day 10, 15 and 30 by use of immunohistochemistry, light- and electron microscopy. Special attention was paid to PV+ somata within dorsal layer II, and the axonal terminals innervating them. The results indicated that PV was expressed in the MEC at P10, but the expression was especially dense in layer II and appeared to follow a dorso-ventral gradient in layer I. At P10, PV+ somata within dorsal layer II appeared immature, with small nuclear indentations and somatic spines, and were contacted by immature-looking PV+ and immunonegative axon terminals. Maturation of both the PV+ cell bodies and the axonal innervation seemed to occur several weeks into the postnatal period. The average number of PV+ axon terminals appeared to overshoot, followed by a period of pruning. Large variations in the number of PV+ axon terminals within each age group indicated that the interconnectivity between MEC PV+ cells may be more intricate than previously thought.

Contents

Abbreviations

General

CA1/2/3 – Cornu ammonis 1/2/3

Calb+ – Calbindin-containing

DG – Dendate gyrus

EC – Entorhinal cortex

EM – Electron microscopy

ER – Endoplasmic reticulum

GABA – γ-aminobutyric acid

HF – Hippocampal formation

HR – Hippocampal region

LEC – Lateral entorhinal cortex

LM – Light microscopy

MEC – Medial entorhinal cortex

P – Postnatal day

PAS – Parasubiculum

PER – Perirhinal cortex

PHR – Parahippocamapal region

POR – Postrhinal cortices

PRS - Presubiculum

PSD – Postsynaptic density

PV – Parvalbumin

PV+ – Parvalbumin-immunoreactive

Reelin+ – Reelin-containing

SUB – Subiculum

Chemical

ABC – Avidin-biotin complex

BSA – Bovine serum albumine

DAB – 3,3´-diaminobenzidine

H_2O_2 – Hydrogen peroxide

HCl – Hydrochloric acid

MeOH – Methanol

NaOH – Sodium hydroxide

OsO_4 – Osmiumtetroxide

PB – Phosphate buffer

PBS – Phosphate-buffered saline

SoAc – Sodium acetate

TBS – Tris buffered saline

Tx-100 – Triton X-100

Introduction

The nervous system has evolved to enable adaptive behaviors and decision making in response to changes in the environment, and accomplishes this by creating an internal representation place. The sense of place gives a perception of the position of the body in the environment. During navigation in the environment, the sense of place is interlinked with a sense of direction and distance, which is based on the integration of movement and knowledge about previous positions. Research has shown that the hippocampal region (HR) is critical for spatial orientation (O'Keefe & Dostrovsky 1971; Fyhn et al. 2004). Understanding the underlying mechanisms of this spatial system have become one of the major goals in modern neuroscience, as such knowledge is expected to yield important insights into the coding of other higher cognitive processes (Moser et al. 2014). Essential to such an understanding is a complete description of the neurons making up its microcircuits, including the functional and structural characteristics of the connections between them.

1.1. The hippocampal region

The HR has been extensively studied over the last century, but there is still confusion regarding the terminology of their various components as well as which regions should be included under which term (Witter & Amaral 2004). Here, I have chosen to adopt the nomenclature suggested by Insausti and colleagues (1997), in which the HR is taken to include the hippocampal formation (HF) and the parahippocamapal region (PHR). The following sections will describe the rodent HR. An overview of the position, subdivisions and interconnection of the rat HR is presented in figure 1.

1.1.1. The hippocampal formation

The HF is a C-shaped cortical structure situated in the caudal part of the brain, with the ventral part bordering with the amygdala and the rostrodorsal part reaching the septal nuclei of the basal forebrain (Witter & Amaral 2004). The long, curved axis of the HF runs along a dorsal (septal)-to-ventral (temporal) axis, referred to as the 'septotemporal axis', and the dorsal and ventral portions have different connectivity with cortical and subcortical areas (Figure 1A; Strange et al. 2014). The cortex that makes up the HF has a three-layered appearance, which is line with the typical organization of the so-called allocortex (van Strien et al. 2009).

The HF comprises three cytoarchitectonically similar regions – the dentate gyrus (DG), the subiculum (SUB) and the hippocampus proper, which is subdivided into cornu ammonis 1 (CA1), CA2 and CA3 respectively (Canto et al. 2008).

1.1.2. The parahippocamapal region

The PHR wraps around the caudal and ventral HF, bordering the subiculum. In contrast to the HF, the PHR is generally described as having six layers (van Strien et al. 2009). The HPR comprise the presubiculum (PRS), the parasubiculum (PAS), the perirhinal cortices (PER), the postrhinal cortex (POR) and the entorhinal cortex (EC; van Strien, Cappaert, & Witter, 2009). Several attempts have been made to subdivide the EC. Based on cytoarchitectonic criteria, it is now generally accepted that the EC can be subdivided into the LEC and the MEC (Witter et al. 1989). Like the HR, the EC follow a dorso-ventral axis (Strange et al. 2014).

1.1.3. Connectivity within the hippocampal region

The subcomponents of the HR are highly interconnected, and largely unidirectional (figure 1B). Grossly, the EC receives most of its neocortical input from the postrhinal cortices, making up two parallel projection streams: the PER projects to the LEC, whereas the POR projects to the MEC. This connection between the EC and the POR is reciprocal. The EC also receives input from the PRS. The major source of cortical input to the HF is formed by cells within layer II and III of the EC. These projections give rise to the the so-called perforant pathway, which distributed to all subregions of the HF. Entorhinal cells of layer II project to the DG, the CA1 and the CA3, whereas entorhinal cells of layer III project to CA1 and the SUB. Furthermore, cells of the DG project via their mossy fibers to the hippocampal CA3. CA3 collaterals project to CA1, and cells within the CA1 project in turn to the SUB. Output from the HF arises in CA1 and the SUB, and is further projected to the PHR, mainly to the deeper layers of the EC. Cells in the deep layers of the EC project to various cortical areas, and might therefore make up a direct hippocampal output route to the neocortex (Insausti et al. 1997).

Different types of spatial information are represented in the HR, and the interconnectivity of HR might facilitate exchange of these different types of spatial information in order to make navigation through the environment possible (van Strien et al. 2009).

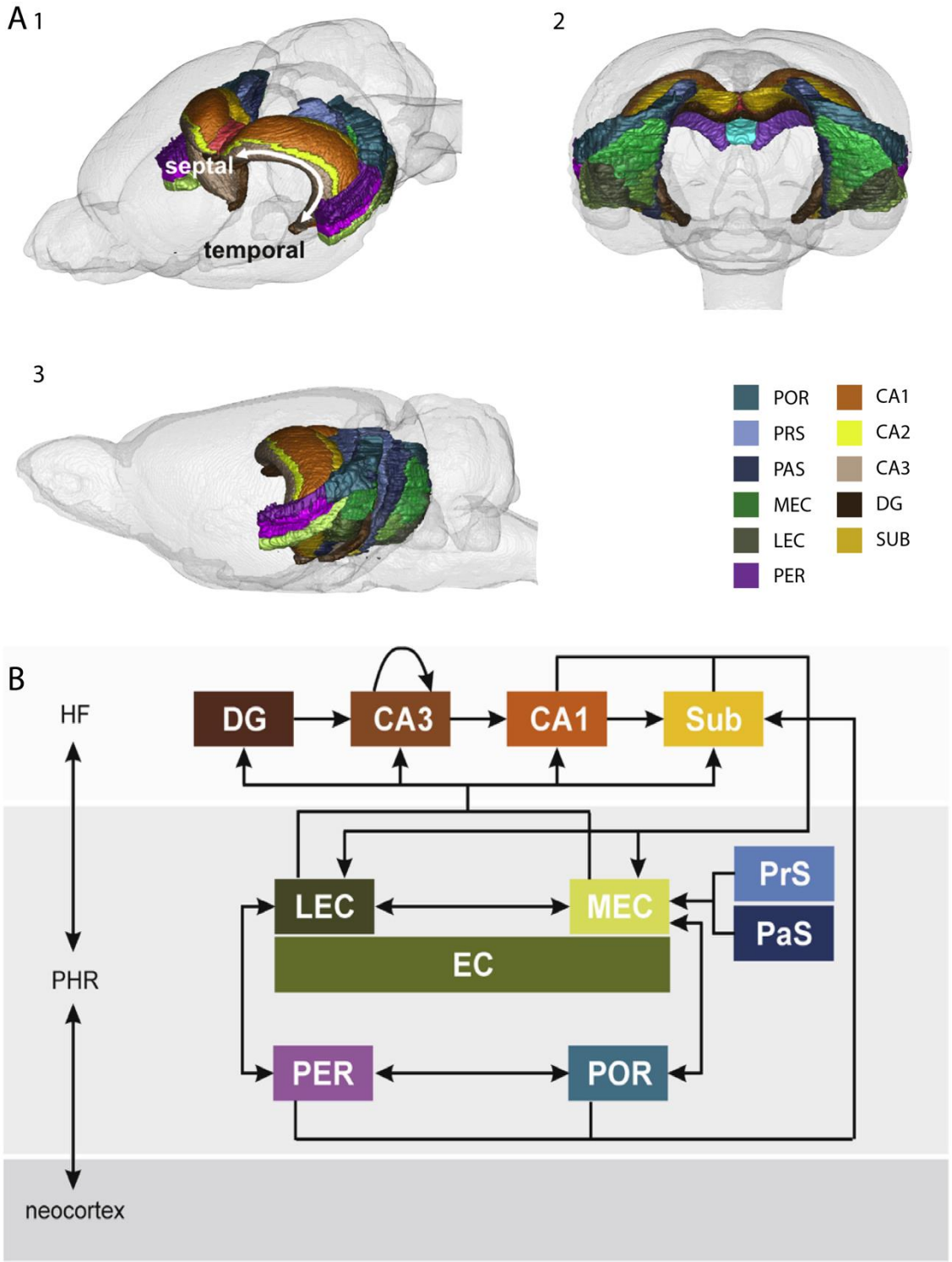

Figure 1: Overview of the position, connectivity and subdivisions of the HR. (A) 3D views of the HR embedded in a rat brain in a (1) rostro-dorsolateral, (2) caudal and (3) lateral view. The septotemporal axis are represented by the white arrow. (B) The standard representation of the HR circuitry. Adapted from Cappaert et al. (2014).

1.1.4. Cells of the spatial system

Intracellular recordings in rodents have shown that the HR comprise several functional cell types that contribute to the the brain´s neural map of space and self-localization within an

environment. These includes ‘place cells’, that fire in response to a specific location in the landscape, located in the HP and DG (Park et al. 2011; O’Keefe 1976). ‘Border cells’ fire in response to border within the landscape, are are found within the MEC and SUB (Savelli et al. 2008; Solstad et al. 2008; Lever et al. 2009). ‘Head-direction cells’ fire in response to the head direction of the animal, and are located in subicular complex and the MEC (Sargolini et al. 2006; Taube et al. 1990). Within the MEC, ‘speed cells’ fire in response to the speed of the animal (Kropff, Carmichael, Moser, & Moser, 2015), and ‘time cells’ code for time (Kraus et al., 2015). Finally, ‘grid cells’ are located in the PRS, the PAS and the MEC (Boccara et al. 2010; Hafting et al. 2005), and their firing fields make up a periodic triangular array covering the entire space available to the animal.

1.2. Spatial activity in layer II of the medial entorhinal cortex

The MEC occupies a more caudomedial portion of the EC and have been found to be involved in spatial processing (Hafting et al. 2005), whereas the LEC occupies a more rostrolateral portion and show little spatial modulation (Hargreaves 2005). This thesis will focus on the MEC.

1.2.1. Grid cells

Grid cells are place modulated neurons that fire at multiple discrete and regularly spaced location, making up a hexagonal pattern that represents the entire environment available to the animal (Hafting et al. 2005). The grid cells can be characterized in terms of three properties; orientation (the tilt of the grid relative to some reference direction), scale (the distance between adjacent firing fields), and spatial phase (displacement in the y and x directions relative to an external point of reference) (Moser et al. 2014). Grid cells are organized in a non-topographical manner, such that the phase of neighboring grid cells are no more similar than those of grid cells recorded at other locations. Grid cells have been found to cluster into modules with cells with similar grid orientation, grid scale and grid spacing (Fyhn et al. 2004; Hafting et al. 2005), and the spacing increase in discrete steps along the dorsal-ventral axis of the MEC (Stensola et al. 2012).

The firing map is dynamical, in the sense that it is driven by the animal´s movement within the environment (Fyhn et al. 2004; Hafting et al. 2005). Only a few sensory input are sufficient to influence the grid firing pattern, and include proprioceptive feedback, vestibular signals and optical flow (Moser et al. 2014). Grid cells maintain their firing maps after

removal of visual and olfactory landmarks (Hafting et al. 2005; Fyhn et al. 2007). Therefore, it is believed to arise intrinsically in the MEC or at another part of the parahippocamapal circuit (Moser et al. 2014).

The MEC has six layers, four of them are cellular (layer II, III, V and VI) and the remaining are plexiform layers (I and IV), with a sparse number of cells (Insausti et al. 1997). Grid cells are most abundant in within layer II (Sargolini et al. 2006), and have therefore been most extensively studied in this layer (Couey et al. 2013; Domnisoru et al. 2013; Giocomo et al. 2007).

1.2.2. Grid cell candidates

The proportion of grid cells within the MEC is currently debated. Research has indicated that grid cells make up 33% (Q. Tang et al. 2014) or 50% (Boccara et al. 2010) of the cell population within layer II of the MEC. The cellular identity of the grid cells is also under debate. Two major principal types are found within layer II: reelin-immunoreactive (reelin+) stellate cells and the calbindin-immunoreactive (Calb+) pyramidal cells. Studies indicate that there is a certain degree of variability within each cell class (Canto & Witter 2012; Fuchs et al. 2015; Klink & Alonso 1997). Whereas some studies claim that the reelin+ stellate cells are the most likely candidates for grid cells in layer II of the MEC (Domnisoru et al. 2013; Burgalossi et al. 2011; Schmidt-Hieber & Häusser 2013), other studies have indicated that it is the Calb+ pyramidal cells (Q. Tang et al. 2014).

1.2.2.1. Pyramidal neurons

Pyramidal neurons make up about 34% of the cells within layer II of the rat MEC (Q. Tang et al. 2014). They are characterized by their triangular somata, a prominent thick apical dendrite that branch at or near the border of layer I, and their immunoreactivity to calbindin. Few apical dendrites and short basal dendrites confined to the superficial portion of layer II and III gives the overall dendritic tree a rectangular appearance. Their somata is mostly located in the deepest part of layer II. Their axon travel via the angular bundle, and axonal collaterals are found within layer I, II and III (Canto et al. 2008).

1.2.2.2. Stellate cells

Stellate cells make up about 53% of the cells within layer II of the rat MEC (Q. Tang et al. 2014). They are defined by a stellate dendritic architecture, distinctive electrophysiological

properties, and their immunoreactivity to reelin (Pastoll et al. 2012). Their perikarya are mostly located in the superficial and middle part of layer II, and their dendritic tree is confined within layer I, II and III. The stellate cells project to the DG and the CA3 (Witter et al. 1989), and axonal collaterals are found within MEC layer I, II and III (Klink & Alonso 1997; Canto & Witter 2012).

1.2.3. Interneurons of layer II

Layer II consists of about 13% interneurons (Q. Tang et al. 2014). They release γ-aminobutyric acid (GABA) at their synapse and axon collaterals are confined within the MEC (Wouterlood & Pothuizen 2000), although GABAergic neurons with long-range projections to the hippocampus have been described (Germroth et al. 1989). Based on a combination of neurochemical markers, morphology and electrophysiological properties, these are classified as multipolar neurons, bipolar cells, basket- and chandelier cells (Canto et al. 2008).

Interneurons characterized by expression of the calcium-binding protein parvalbumin (PV) has recently received increased attention due to their involvement in the regulation of grid cells.

1.3. Parvalbumin-expressing cells of the grid cell network

1.3.1. Regulation of grid cell firing

Several studies indicate that parvalbumin-immunoreactive (PV+) cells regulate the grid cell firing. First, by use of optogenetics and tetrode recordings in mice, Buetfering and colleagues (2014) recently showed that individual PV+ cells receive strong excitation from grid cells with various phases. While the PV+ cells did not exhibit any grid cell-like firing themselves, they robustly inhibited the firing activity of the grid cells. Second, by use of a combination of electrophysiological, optical and morphological circuit analysis on rats, Beed and colleagues (2013) showed that layer II stellate cells are controlled by strong inhibition. The frequency of spontaneous inhibitory postsynaptic currents decreases significantly from dorsal to ventral, similarly to the grid spacing, and stellate cells in dorsal layer II receive a greater number of inhibitory inputs than ventral layer II stellate cells. By use of immunofluorescence, they showed that the density of PV+ axon terminals decrease from dorsal to ventral, indicating that inhibition from PV+ cells are involved in regulating of the grid firing pattern along the dorso-ventral gradient (Beed et al. 2013). Third, by use of patch-clamp recordings in mice,

Gonzalez-Sulser and colleagues (2014) showed that long-range GABAergic projections from the medial septum to the MEC is required for grid cell firing. Interestingly, this projection occur via synaptic coupling to fast-spiking interneurons in layer II, demonstrating the important role of fast-spiking PV+ cells in the grid firing pattern (Gonzalez-Sulser et al. 2014). Taken together, these studies suggests that the inhibition provided by PV+ cells are important component in the making of the grid firing pattern.

1.3.2. Ways of regulating principal cells

Interneurons can regulate activity of connected principal cells or provide feed-forward inhibition, in which an interneuron receive excitatory input and exert inhibitory output onto a connected principal cell (Mittmann et al. 2005). Interneuron activity can also provide feedback-inhibition, in increased activity in a principal cell elevate the activity of a interneuron, which in turn may decrease the activity of the principal cell (Buzsáki 1984). Finally, interneuron activity might result in disinhibition of an excitatory cell if two GABAergic neurons are linked in a simple serial circuit (Jones & Bühl 1993) or self-inhibition of the interneuron if it is self-connected via a so-called autapse (Van der Loos & Glaser 1972; Deleuze et al. 2014).

1.3.3. Physiology

PV+ cells within the MEC have been identified as fast-spiking cells (Jones & Bühl 1993), and electrophysiological properties are similar to what have been reported in various brain regions (Sik et al. 1995; DeFelipe et al. 2013; Freund & Buzsáki 1998).

The term ‘fast-spiking’ refer to the brief duration of action potentials and high frequency at which these can be discharged with little or no frequency accommodation (Jones & Bühl 1993). Fast-spiking PV+ cells have weakly excitable dendrites, which allow them to sample activity in the surrounding network, and a highly excitable axon, which enable fast propagation of the signal to a large number of cells (Hu et al. 2014).

Serially-coupled PV+ cells play a key role in the generation of gamma oscillations in the EC (Bartos et al. 2007). Previous studies have indicated that their fast-signaling properties are necessary to provide frequency tuning and to optimize synchronization of network oscillations in the gamma range (Bartos et al. 2001; Buzsáki & Draguhn 2004; Vida et al. 2006). There is a pronounced dorso-ventral gradient in the power of gamma oscillations within the rat MEC (Beed et al. 2013). A key property of fast-spiking PV+ cells is that they

can fire action potentials at a high frequency with little accommodation (Buhl et al. 1994; Kawaguchi 1995).

1.3.3. Parvalbumin-expressing cells within layer II

About half of the GABAergic neurons within the EC contain PV (Miettinen et al. 1996), and are found within all layers of the MEC, with the exception of layer I. PV+ somata are small or medium sized with different shapes. A prominent feature of these neurons are the extensive dendritic arborization in various directions (Wouterlood et al. 1995).

The dendrites of cells within layer II ramify within layer II and into layer I. Their axons are confined within layer II and III (figure 2A; Canto et al. 2008), are unmyelinated and form asymmetrical synapses (i.e. inhibitory) on their postsynaptic targets (Wouterlood et al. 1995; Soriano et al. 1993). PV+ cells within layer II of the MEC have been identified as basket- and chandelier cells (Wouterlood et al. 1995; Soriano et al. 1993).

1.3.3.1. Basket cells

Basket cells are characterized by their extensive axonal arbor, that form baskets of terminals mainly around the soma and the proximal dendrites of their target cell (Jones & Bühl 1993; Figure 2B). The large number of *en passant* terminals arise from the axonal arbor, which permits the PV+ cell to generate a divergent, fast and synchronous transmitter release, and thus effectively control the output of their target cell (Hu et al. 2014).

1.3.3.2. Chandelier cells

Chandelier cells are characterized by the vertical aggregation of axonal terminals, called candles, that innervate the axonal initial segments of their target cells (Figure 2A; Seress & Ribak, 1990). Two distinct forms of cell types can be distinguished on the basis of their axonal arborization. One type extend their axons along layer II and III, whereas the other exhibit smaller and horizontally oriented axonal complexes (Soriano et al. 1993).

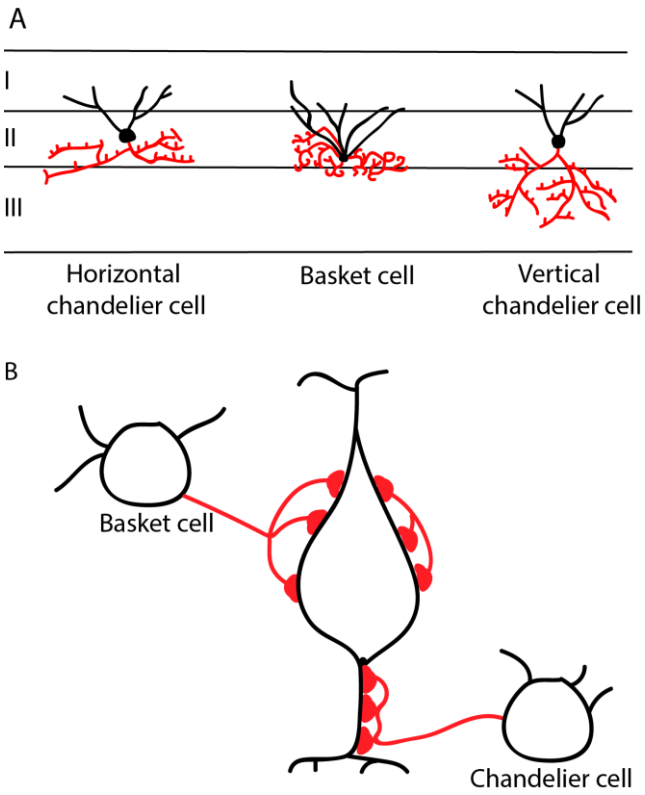

Figure 2: Illustration of (A) PV+ cell types within layer II of the MEC, and (B) how they innervate the perisomatic region of their target cells. Axons are shown in red, while dendrites are shown in black. Figure A inspired by Canto et al. (2008).

1.3.4. Connectivity within layer II of the medial entorhinal cortex

Because their recruitment is strongly constrained by their afferent innervation, and the impact of their activity within the network is strongly related to their efferent output, the PV+ cells within MEC layer II needs to be understood in the context of the circuit they contribute to. Knowledge about their connectivity is however limited. A summary of identified afferent and efferent connectivity of PV+ cells within layer II of the MEC is shown in figure 3.

A combined immunohistochemical and electron microscopic (EM) study have shown that PV+ cells within layer II of the MEC receive synaptic input on their somata and on the dendrites ramifying into layer I and III (Wouterlood et al. 1995). Both dendrites and the cell bodies are densely covered by afferents forming symmetrical (i.e. inhibitory) and excitatory asymmetrical (i.e. excitatory) contact (Wouterlood et al. 1995). Some of these axon terminals are PV+, and arise from other PV+ cells within the MEC. Indeed, PV+ within the MEC make form numerous synaptic connections with each other, mostly on the perisomatic region (Wouterlood et al. 1995). PV+ afferents could also arise from self-innervation, as fast-spiking basket cells have been found to self-innervate in other regions of the brain (Tamás et al. 1997;

Bacci et al. 2003). As mentioned previously, PV+ somata within layer II also receive long-range GABAergic projections from the medial septum (Gonzalez-Sulser et al. 2014). Further, pair recordings have shown that about a quarter of all PV+ cells within layer II are excited by stellate cells, and about half are exited by cells intermediate to that of stellate- and/or pyramidal cells (Fuchs et al. 2015). Because the latter study did not include immunohistochemical technics, it is not known whether these intermediate cells expressed calbindin or reelin. Further, because information obtained by electrophysiological studies cannot determine anything about the specific place of innervation, they cannot easily be related to observations about afferent innervations at EM.

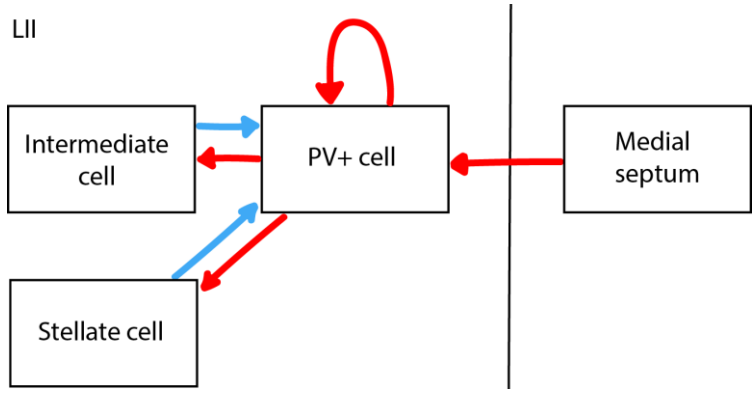

Figure 3: Summary identified connections to and from PV+ cells in layer II (LII) of the MEC. Excitatory inputs are shown in blue, while inhibitory inputs are shown in red.

PV+ cells within layer II of the MEC make numerous contacts on stellate cells and those intermediate to stellate and/or pyramidal cells (Fuchs et al. 2015). With a combination of electrophysiology and immunohistochemistry for confocal microscopy, Armstrong and colleagues (2015) recently showed that an individual PV+ basket cells could innervate both reelin+ and Calb+ cells simultaneously, but each individual PV+ cell varied in terms of proportion of bouton on the respective principal cells. Because the reelin+ principal cells project to the ipsilateral DG via the perforant path and Calb+ principal cells project to other non-DG brain regions (Varga et al. 2010), the study indicated that the PV+ basket cells were selective for principal cell types with respect to their divergent output of the MEC. By use of EM and immunohistochemistry, it has been shown that PV+ cells make numerous synaptic contact on each other (Wouterlood et al. 1995).

Because connectivity must be present before a system is functional, knowledge about the development of the medial entorhinal cortex is essential.

1.3.5. Development of layer II of the medial entorhinal cortex

While a large body of research have focused on development of the HF, the literature on postnatal development of the MEC is sparse. By use of immunohistochemistry, Ray and Brecht (2016) have shown that principal neurons within layer II are present at birth. Principal neuronal types described in adult rats can be observed in young rats already from postnatal day (P) 14, with respect to both electrophysiological and morphological features (Canto & Witter 2012).

Whereas development of PV+ cells have been readily described in the rodent HF, PV+ cell development within the MEC has only been described briefly in primates. Within the human MEC, no PV+ cells were present until the fifth postnatal month, and developed first within layer III (Grateron et al. 2003). Within the monkey MEC, PV expression develop according to a medial-lateral gradient, PV expression were present before birth, and first observed in layer III and V (Berger et al. 1993; Grateron et al. 2003).

The functional developmental properties of grid cells have also been investigated, and a rudimentary map of space has been found present at the time rats opened their eyes and left the nest for the first time, at P14 to18. However, adult-like grid responses were not recorded earlier than P20 and the coherent grid network continued to emerge from P25 onwards (Langston et al. 2010; Wills et al. 2010). Little is known about the structural development of the microcircuits which bring about these properties, including PV+ cells.

1.4. Aim

The PV+ cells are essential for proper function of the entorhinal- and spatial network, but knowledge about their function and interconnectivity within the entorhinal microcircuitry is sparse. Knowledge about their morphology and connectivity during development is an important approach to gain a better understanding about their function.

The aim of this thesis is to investigate the postnatal maturation of PV+ cells within the rat MEC at P10, P15 and P30 by use of immunohistochemical processing for light microscopy (LM) and EM. Morphological characteristics and distribution of PV+ cells will be described across layers at the level of LM, and the ultrastructure of the perisomatic region and the afferent input to the perisomatic region of PV+ cells within the dorsal part of layer II at the level of EM. Special attention will be given to maturation of PV+ afferent input.

2. Materials and methods

Several protocols for immunohistochemistry and tissue preparation for EM were tested to obtain optimal results. The final protocols that achieved best results are described in the following section, whereas other tests and their results will be described in section 3.1. Images, detailed protocols and recipes for solutions are given in appendix I, II and III respectively. Unless otherwise specified, the pH of the solutions was 7.4-7.5, the molarities of the buffers was 0.1 and MilliQ water was used to dilute solutions. All of the washing and incubation steps took place on a shaker. Controls of the immunohistochemical processing for both LM and EM were done without the primary antibody, and showed no expression of PV.

2.1. Animals

In total 19 in-house bred Long-Evan hooded rats (16 males and 3 females) from the Kavli Institute of Neuroscience were used in this study at P10 (N = 4), P15 (N = 4), P20 (N = 2), P30 (N = 6) and P90 (N = 3). All rats were subject for immunohistochemical testing, and rats from P10, P15 and P30 were used for the final experiments. Five male rats at P10 (N = 1), P15 (N = 2) and P30 (N = 2) were used for LM, whereas four male rats at P10 (N = 1), P15 (N = 1) and P30 (N = 2) were used for EM. Possible variations in the number of immunoreactive terminals and morphology resulting from differences between brain hemispheres was avoided by using only left hemispheres in the EM preparations. All animals were treated in accordance with regulations given by the Norwegian Animal Research Authority (NARA).

2.2. Perfusion and tissue sectioning

All rats were anaesthetized with 4-5% Isoflurane, and rats at P20 and older were subsequently injected with an overdose of pentobarbital. Absence of reflexes was used as an indicator that animals were completely anaesthetized. The rats were then perfused using 4% paraformaldehyde and 0.1% glutaraldehyde in phosphate buffer saline (PBS) via the vascular system.

To preserve the structure and to protect the tissue against subsequent treatments, the brains were immediately put into the same fixative after removal from the skull and post-fixed for a period between 1 week (LM) and two weeks (EM) before sectioning. Morphological tests were performed on all rats at P10, P15 and P30, and demonstrated in all cases that the tissue was in good condition.

Brains subject for LM proved to be fragile during sectioning which resulted in sections of uneven thickness, possibly because of shorter fixation time, and was therefore immersed in 10% porcine skin gelatin in Sørensens phosphate buffer for 30 minutes at 37°C followed minimum 30 minutes at 4°C before sectioning. This was not necessary for brains subjected for EM. For each brain, sagittal sections of the MEC and surrounding areas were cut using a vibratome (Leica VT 1000S) with brains immersed in a cold PBS bath. The thickness was 35µm for LM and 60µm for EM. Vibratome sections used for EM were post-fixed overnight at 4°C in 4% paraformaldehyde, 0.1% glutaraldehyde in PBS. All vibratome sections were stored in PBS at 4°C until further immunohistochemical processing three weeks later.

2.3. Immunohistochemistry for light microscopy

The vibratome sections were first washed 3x15 minutes in PB, followed by a permeabilization in PB containing 1% Triton X-100 (Tx-100) for 2x10 minutes to permeabilize the cell membranes. Blocking for endogenous peroxidase activity were done by incubating the tissue in 1% hydrogen peroxide (H_2O_2) and 50% methanol (MeOH) in PB for 30 minutes, followed by another 3x15 minutes wash in PB. To block for non-specific antibody binding, the sections were then pre-incubated in PB, 1% Tx-100 and 5% normal horse serum (Sigma, H0146) for 60 minutes, before incubation with the primary antibody (polyclonal goat anti-Parvalbumin, Swant, PVG-214) diluted to 1:40 000 in PB, 1% Tx-100 and 5% normal horse serum for 22 hours at 4°C.

Following these steps, the tissue was rinsed in PB before being incubated with the secondary antibody (biotinylated anti-goat IgG raised in horse, Vector laboratories, BA-9500) diluted to 1:200 with PB and 1% Tx-100 overnight at 4°C. Following a 3x15 minutes rinse in PB, the sections were incubated with avidin-biotin complex (ABC; Vector laboratories, BA2001) for 1 hour to increase the detection sensitivity. Next, the sections were washed for 3x15 minutes in PB, and subsequently stained in the dark with 0.05% 3,3`-diaminobenzidine (DAB) and 0.01% H_2O_2 in PB to produce a dark brown precipitate in cells expressing PV. After 8 minutes, the DAB reaction was stopped with a 3 x15minutes rinse in PB, and the sections were subsequently washed 2x10 minutes in MilliQ water, mounted on glass slides (thermo scientific, menzel-gläser) and dried at room temperature for 30-40 minutes. Finally, the sections were coverslipped with mounting medium and dried in a fume hood overnight.

2.4. Immunohistochemistry for electron microscopy

Every step up to the DAB staining was initially the same for EM as for LM, except from the following

- The Tx-100 concentration was 0.05% instead of 1%
- One washing step was repeated 5x7 minutes instead of 3x15 minutes
- A washing step was included between permeabilization and blocking
- The sections were pre-incubated in 1% bovine serum albumine (BSA) 1% normal horse serum in PB and 0.05% Tx-100 for 90 minutes, instead of PB and 1%Tx and 5% normal horse serum for 60 minutes. P10 sections were pre-incubated without Tx-100
- The primary antibody was diluted in 1% BSA, 1% normal horse serum and PB instead of 1% Tx-100 and 5% normal horse serum and PB
- The secondary antibody was diluted to 1:400 with PB instead of 1:200 with PB and 1% Tx-100, and incubated for 2 hours in room temperature instead of overnight at 4°C
- The concentration of DAB was reduced to 0.03% instead of 0.05%, and the sections was stained with DAB for 5 (P15 and P30) and 8 (P10) minutes

After DAB staining, the sections were further inspected for labeling in a light microscope (Zeiss Axiophot) and subsequently transferred to sterile wells. All equipment from this step to secondary fixation was rinsed in 10% hydrochloric acid (HCl). Next, the sections were washed 3x10 minutes in 2% sodium acetate (SoAc; pH 8.7) diluted in boiled MilliQ water, and subsequently incubated with 10% sodium thioglycolate diluted in boiled MilliQ water overnight (13.5 hours) at 4°C to block for unspecific labeling during silver enhancement.

The sections were further washed in 3x10 minutes in 2% SoAc (pH 8.7) before being incubated in a silver developmental solution for 7-8 minutes in the dark (recipe for the silver developmental solution can be found in appendix III). The silver enhancement reaction was stopped with a 2-minute wash in 1% acetic acid, and the sections were subsequently washed 3x10 minutes in 2% SoAc (pH 8.7). To allow the site of the antigen localization to be readily visualized, the sections were incubated with 0.05% gold chloride ($AuCl_3$) for 15 minutes in the dark before being washed 3x10 minutes in 2% SoAc (pH 8.7), rinsed in 3% sodium thiosulphate for 10 minutes, followed by another 3x10 minutes wash in 2% SoAc (pH 8.7).

2.5. Electron microscopy preparations

The sections were then transferred to dram glass vials, washed in cacodylate buffer in 2x10 minutes, and subsequently fixed in 1% osmiumtetroxide (OsO_4), 1.5% potassium ferrocyanide and cacodylate buffer for 15 minutes in the dark to enhance lipid contrast. Following these steps, the sections were washed in cacodylate buffer, dehydrated with an increasing concentration of ethanol; 50%, 70% and 90% x 10 minutes and 100% for 4x15 minutes. Next, the sections were incubated in 100% acetone for 2x15 minutes, and subsequently infiltrated with an increasing concentration of epoxy resin in acetone: 2+1 for two hours, 1+1 for two hours, 1 + 2 overnight on a rotator. 0.15 ml accelerator DMP-30 were added to the Tx-100 prior to use. Next, the sections were infiltrated with pure epoxy for 6+2 hours on a rotator.

Finally, the sections were flat-embedded in epoxy between two sheets of aclar film and two glass slides at 60°C overnight (11.5 hours) to allow polymerization of the epoxy. The dorsal portion of the MEC was identified on the basis of differences in staining intensity between the MEC and the PER (Boccara et al. 2015), selected by use of a stereo microscope, carefully dissected from the vibratome sections (figure 4), mounted on epoxy blocks with fresh epoxy and left to harden in 60°C for 3 days.

The epoxy blocks were trimmed with a razor blade. 500nm thick sections of the tissue were cut with an ultramicrotome (Leica EM UC6) in a MilliQ water bath and subsequently stained with Toluidine Blue to identify PV+ cells within layer II. After identification of PV+ cells, the block was trimmed with a razorblade to form a trapezoid cutting face. 55-60nm thin sections containing layer I, II and III of the most dorsal portion of the rostro-caudal MEC were cut from the epoxy-blocks with a Diatome diamond knife, and subsequently collected on 200 mesh thinbar copper grids. To enhance contrast, the sections where put on drops of 4% uranyl acetate and 50% ethanol for 8 minutes in the dark, and 1% lead citrate diluted in sodium hydroxide (NaOH) for 3-4 minutes before the reaction was stopped in MilliQ water.

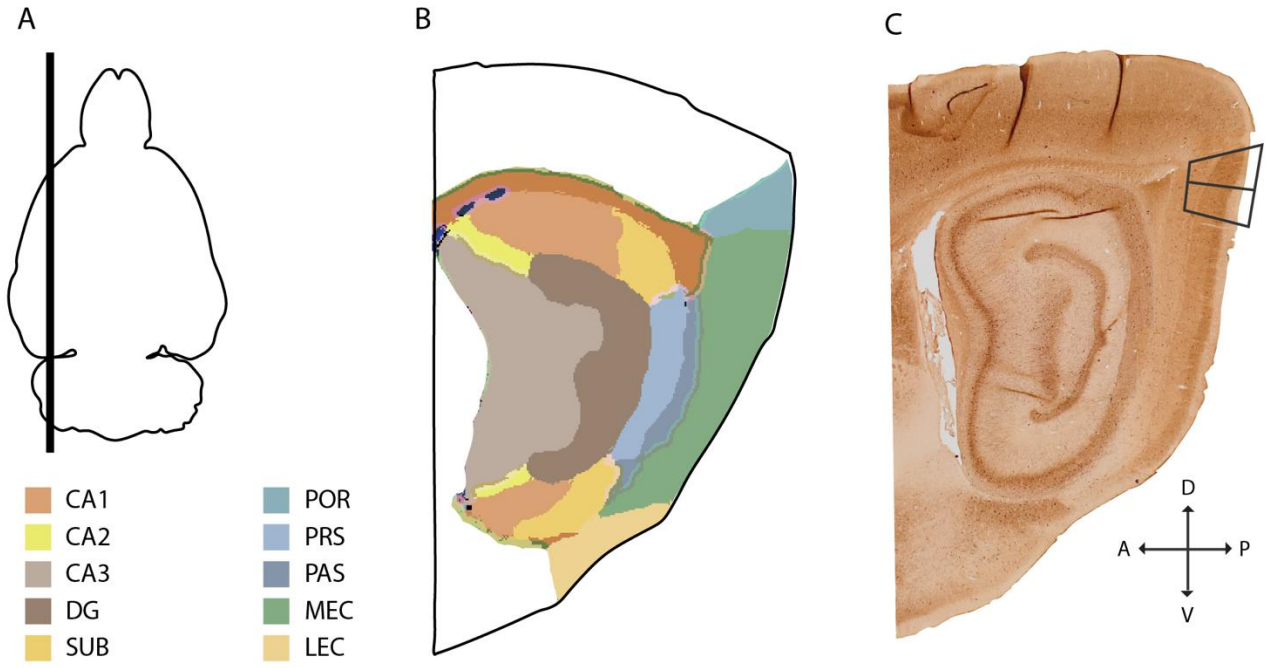

Figure 4: Illustration of the area selected for EM processing. (A) Horizontal section of the rat brain. The black line corresponds to the sagittal sections shown in B and C. (B) Sagittal section of the rat hippocampal region with color codes of the various subdivisions. (C) Light micrograph indicating the areas of the MEC selected for EM (sagittal section). D = dorsal; P = posterior; V = ventral; A = anterior. Figure derived from Boccara et al. (2015) and Yushkevich et al (2006).

2.6. Analysis

2.6.1. Light microscopic sampling

Vibratome sections were scanned with an Olympus VS120 Virtual Slide Microscope at a magnification of x10 objective for the whole section and x40 objective for the MEC. Images were captured with VS-ASW program and processed with OlyVIA 2.8 (Olympus). Two sagittal vibratome sections from each animal were subject for analysis. The morphological description and categorization of PV+ cells within layer II was based on the nomenclature proposed by Ascoli and colleagues (2008). Size of cell bodies was measured within layer II, on somata with a visible nucleus and that were located half way down the dorso-ventral-axis. The long and short axis of the PV+ cells at P10 (N = 64), P15 (N = 41) and P30 (N = 41) were measured with OlyVIA 2.8 (Olympus), and adjustments of brightness (+14) and contrast (+4) were performed on all light micrographs.

2.6.2. Electron microscopic sampling

EM sections were examined with a transmission EM (JEOL JEM-1011), electron micrographs were captured at x8.000, x15.000 and x25.000, and analyzed with iTEM 5.0. One vibratome section from P10 and two from each animal at P15 and P30, were subject for immunohistochemistry, and the dorsal portion of the MEC were subsequently processed for EM. Two tissue blocks were made from each vibratome section.

For each age group, five PV+ cells within dorsal layer II of the MEC were followed for eight to nine thin sections. Contrary to layer III, layer I of the were easily distinguished from layer II on the basis of a lack of cell bodies. To ensure the selected PV+ cell bodies were confined within layer II of the MEC, PV+ cell bodies located in the more superficial part of the layer were sampled for analysis. To ensure that the examinated area of the PV+ cell bodies were relatively similar, it was desirable to select cells with a visible nucleus. However, since the number of PV+ cells within one thin section was sparse (0-3), the labeling was densest near the surface of the vibratome section, and because several PV+ cells were had to be excluded from the study because they were repeatedly located behind grid-bars, some of the P15 (N = 3) and P30 (N = 1) cells used for the analysis did not display a nucleus.

The area and perimeter of the soma, nucleus and PV+ terminals were measured for each cell per thin section. Symmetrical and asymmetrical synapses were identified on the basis of the description by Colonnier (1968). Axon terminals was regarded PV+ if they contained labeled grains at around 10 μm and the surrounding tissue did not display unspecific labeling.

All synaptic contacts (PV+ and immunonegative) on the PV+ somata were counted per cell body per thin section. PV+ axon terminals were additionally named and the position of their innervation were documented for each thin section, such that each terminal could be followed through several thin sections, and the number of PV+ terminals per thin section and the number of individual PV+ terminals innervating each cell could be obtained. To calculate the density of PV+ axon terminals (number per μm^2 membrane), the number of PV+ axon terminals per thin section were divided by the perimeter of the soma per thin section. Density of total number of innervating axon terminals (PV+ and immunonegative; number per μm^2 membrane) were calculated by dividing the number of all axon terminals per thin section by the maximal perimeter of the soma for each thin section.

Lysosomes and mitochondria were counted for each soma per thin section. The density of lysosomes (number per μm^2 cytoplasm), were found by subtracting the area of the

nucleus from the area of the soma, and divide the number of lysosomes per thin section by this value. The same procedure was used to determine the density of mitochondria (number per μm^2 cytoplasm). Mitochondria were additionally counted and measured within each PV+ axon terminal per thin section. Although the precise number of synaptic vesicles was not counted, attention was paid to the distribution and density of presynaptic synaptic vesicles per axon terminal per thin section.

To separate between individual somatic spines, they were named and their position on the PV+ cell body were documented for each thin section, such that they could be followed for several section. Identification of axons were based on the description of PV+ cells within the adult MEC (Wouterlood et al. 1995): by the presence of microtubules and by a dense undercoating of the limited plasma membrane.

3. Results

To improve the legibility of this thesis, the abbreviation ‘PV+’ have been left out on several occasions. Unless explicitly indicated, it is referred to PV+ neurons, cell bodies, dendrites, axons and presynaptic terminals when ‘neurons’, ‘cell bodies’, ‘axons’, ‘dendrites’ and ‘terminals’ is mentioned.

3.1. Methodological tests

3.1.1. Immunohistochemistry for light microscopy

Tests for the immunohistochemical processing for LM had to be performed, initially to overcome problems with poor staining. The final protocol was described in section 2.3, and the following protocols can be found in appendix II. Images from the tests can be found in appendix I.

The original immunohistochemical protocol for LM was initially the same as the original protocol for EM (appendix II protocol D). For the first immunohistochemical test subjected for LM, cell bodies were heavily stained whereas dendrites and axons were poorly stained (appendix I figure 11A). We decided to test a regularly used protocol from the Kavli Institute (appendix II protocol A). As this protocol was initially used for immunofluorescence labeling, it was necessary to make a few modifications because we stained with DAB instead of fluorochrome (appendix II protocol B). The major changes from the original to the new protocol were the following:

- PB was used instead of tris buffered saline (TBS)
- PB and 1% Tx-100 was used to permeabilize the cell membranes instead of sodium borohydride
- Tx-100 concentration was increased from 0.05% to 1%
- Primary antibody concentration was decreased from 1:20 000 to 1:40 000
- Pre-incubation and dilution of the primary antibody was done with PB, 1% Tx-100 and 5% normal horse serum, instead of an incubation medium(*) composed of BSA, glycine, lysine monohydrochloride, cold water fish gelatin, 0.05% Tx-100, TBS and 10% normal horse serum
- The secondary antibody was diluted with PB and 1% Tx-100 instead of the incubation medium(*), and the incubation time was changed from two hours at room temperature to overnight at 4°

These changes resulted in selective PV expression in all of the cellular compartments, but the labeling was weak. In the next trial, the DAB reaction time was increased to 8 minutes instead of 4 minutes, and the secondary antibody concentration was increased to 1:200 instead of 1:400. These steps resulted in stronger expression of PV (appendix I figure 11B), and was added to the final protocol.

3.1.2. Immunohistochemistry for electron microscopy

Several tests for the immunohistochemical processing for EM had to be performed, initially to overcome problems with background staining, poor morphology and age specific requirements. The final protocol was described in section 2.4, and the following protocols can be found in appendix II. Images from the tests can be found in appendix I.

The original immunohistochemical protocol for EM resulted in background labeling (appendix I figure 12; appendix II protocol D). Because the new immunohistochemical protocol for LM had been successful, we decided to adapt this protocol for EM processing. The major changes from this adaption was the same as those already described in section 3.1.1, with exception of Tx-100. Tx-100 solubilizes membrane proteins, and might have an effect on the membrane structure and hence the PV labeling. Because of this, the concentration of Tx-100 was kept to 0.05% as in the original EM protocol. The results from the EM test showed no background staining labeling. However, the labeling was very dense and the cellular membranes were poorly defined (appendix I, figure 13A, C, E), which made it very difficult to identify terminals that contacted the somata. A morphological test confirmed that this was not the perfusion or fixation of the animal, but most likely an overexposure to Tx-100. Due to a limited amount of time, rats at P20 and P90 were not processed in further experiments.

With the aim of finding a balance between good morphology and labeling density, a immunohistochemical test was first carried out for LM. Three different conditions with Tx-100 was tested: no Tx-100, 0.05% Tx-100 only during permeabilization, 0.05% Tx-100 during both permeabilization and pre-incubation. Additionally, different concentrations of the primary antibody were tested: 1:20 000 and 1:40 000. The latter concentration resulted in the most optimal PV labeling, and was added to the final protocol. Tx-100 during only during permeabilization appeared to give the most optimal result, and an EM test were subsequently carried out with this modification. The EM test showed that Tx-100 during permeabilization

were sufficient for good labeling P10, but not for P15 and P30 as the labeling was limited to the edge of the sections (appendix I, figure 14). This was interpreted as a result of too little Tx-100 for P15 and P30, such that the antibody could not penetrate the cell membranes properly. Because myelin acts as barrier for antibodies (Rockland 2016), antibodies might penetrate easier into material of P10 because the myelin is not properly developed at the time.

To improve the permeabilization of the membranes while maintaining the good morphology for P15 and P30, another EM test was performed. Here, Tx-100 we tested for 0.05% Tx-100 during both the permeabilization and pre-incubation step, and the pre-incubation time was increased to 90 minutes instead of 60 minutes (appendix II, protocol E). These changes resulted in sufficient membrane visualization and labeling for both P15 and P30 (appendix I, figure 13B, D, F).

3.2. Light microscopic observations

3.2.1. Parvalbumin expression within the medial entorhinal cortex

With the exception of LI, PV expression was observed in all layers of the MEC at P10. PV+ somata and dendrites were most densely labeled within layer II whereas only sparse labeling was observed in layer V/VI. The dendritic processes appeared generally shorter, less arborized and exhibited regional differences (figure 5A). The highest dendritic density was found within layer I, II and III, where the dendrites extended across layers and in all directions. The dendritic arborization appeared highest within layer II, such that it could easily be distinguished from layer III. Layer I displayed several dendrites reaching the pial surface, and within this layer the density gradually decreased from dorsal to ventral.

Whereas there were no apparent changes in the density of cell bodies in layer II, III and IV at P15, there appeared to be an increase in somatic density within layer V and VI (figure 5B). The dendritic arborization appeared generally higher and more arborized within this age group, and the morphology looked generally more mature. Within layer I, the dendrites did no longer follow a dorsal-to-ventral gradient, and the dendrites within layer III appear to exhibit the same density as within layer II such that the distinction between the two layers was more unclear than at P10. At P15, it was also possible to identify terminal boutons, characterized by varicosities forming basket terminals around immunonegative cell bodies (figure 5B). These were most abundant within the superficial layers, but could also be

identified within the deeper layers. Terminal boutons around PV+ cell bodies could not be identified at this magnification.

Compared to P10 and P15, the dendritic arborization and the number of cell bodies appeared increased within layer V and VI (figure 5C).

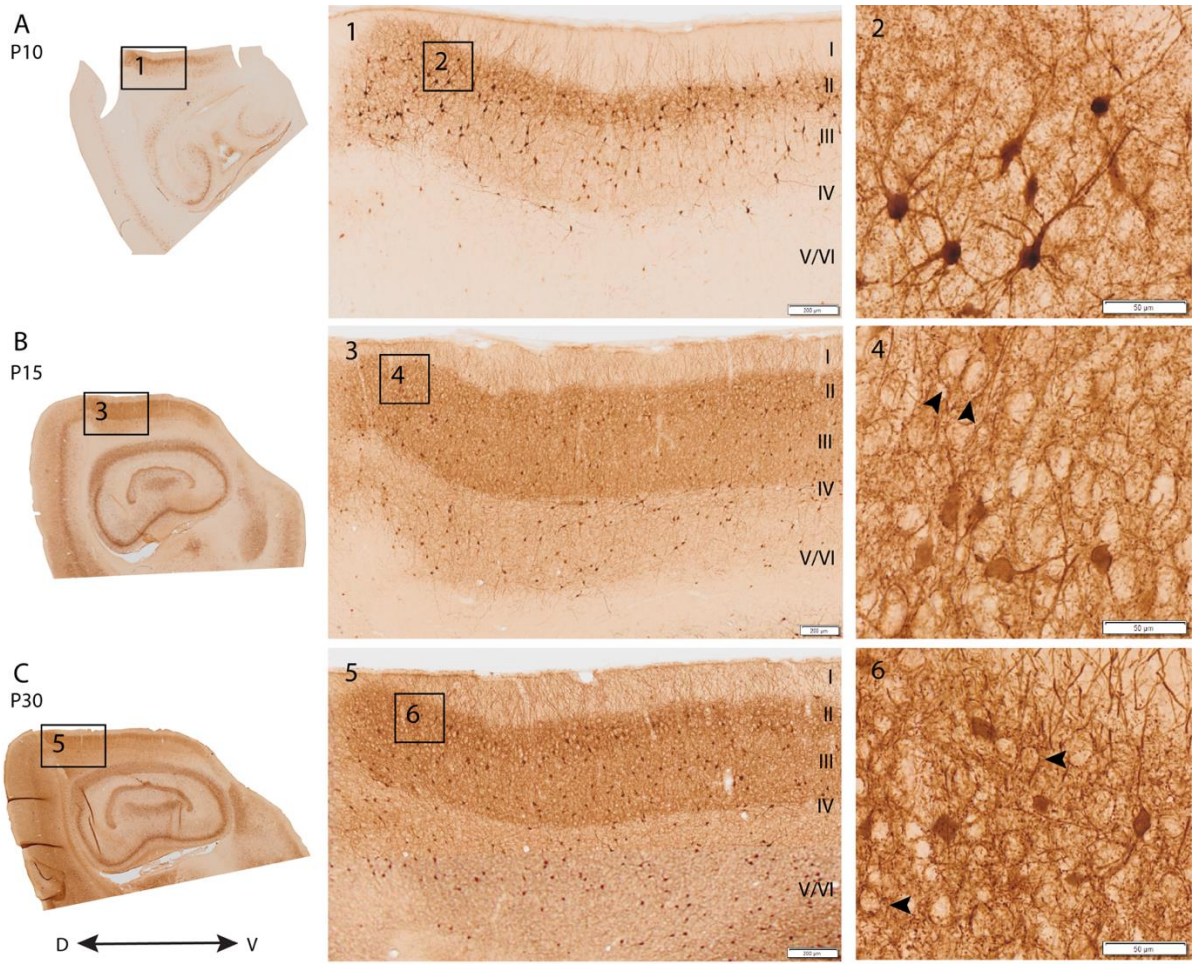

Figure 5: Light micrographs illustrating the density and distribution of cell bodies and dendrites within the developmental MEC at (A) P10, (B) P15 and (C) P30. Layers are indicated with roman numbers. Arrows indicate PV+ axon terminals forming baskets around immunonegative cell bodies. Sagittal sections. Scale bar 200µm (1, 3, 5) and 50µm (2, 4, 6). D = dorsal, V = ventral

3.2.2. Morphology of parvalbumin-expressing cells within layer II

Regardless of age group, the neurons were oriented irregularly and their dendrites appeared aspiny. The dendritic arborization appeared mostly multipolar, with two to four primary dendrites emerging from the soma in various directions. Most branching dendrites did so close to the soma. The cell bodies were mostly round or polygonal, and more rarely shapes

that were not described by any of these terms, such as fusiform (figure 6). The shape of the cell bodies appeared more homogenous at P15 and P30 compared to P10.

The size of the somata varied within each age group, and the mean size appeared to increase with the age of the animal. For P10, the long axis of the cell bodies ranged from 11 to 24µm (mean 16µm) and the short axis ranged from 6 to 18µm (mean 11µm). For P15, the long axis ranged from 14 to 26µm (mean 19µm) and the short axis ranged from 8 to 19µm (mean 12µm), whereas for P30, the long axis ranged from 12 to 26µm (mean 19µm) and the short axis ranged from 9 to 18µm (mean 13µm).

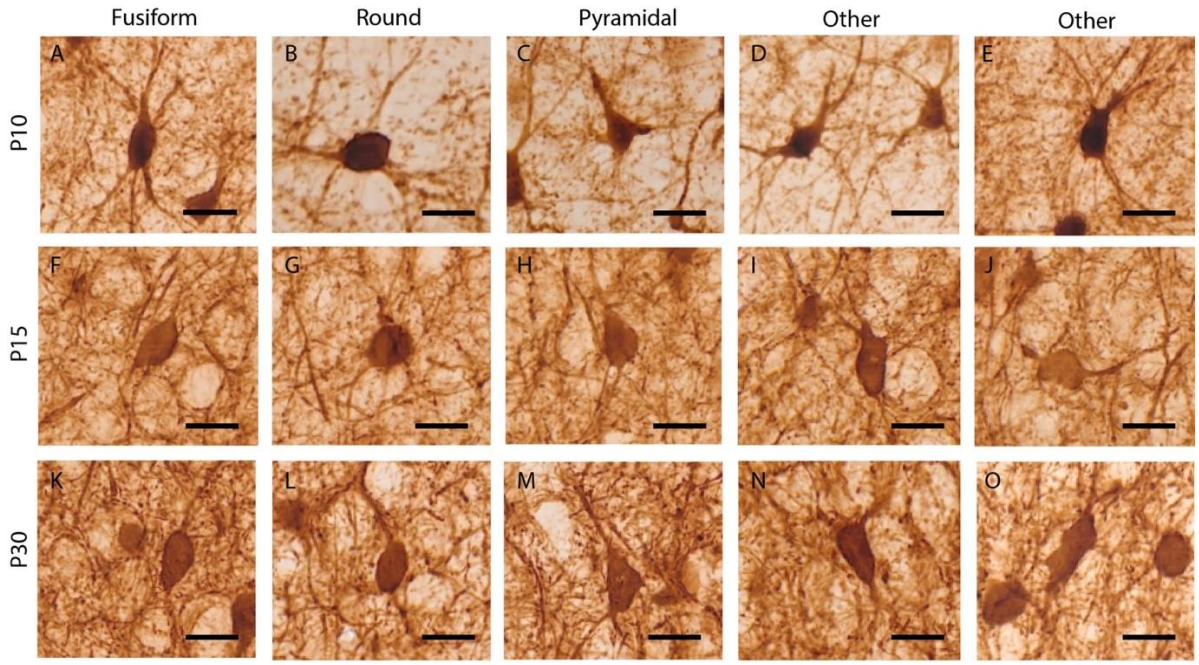

Figure 6: Light micrographs illustrating various shapes of PV+ cell bodies within MEC layer II at P10 (A-E), P15 (F-J) and P30 (K-O). Somata with a fusiform (A; F; K), round (B; G L) and pyramidal (C; H; M) shape were found within all age groups. Cell bodies that were not described by any of these terms (D; E; I; J; N; O) were also identified within all age group. Scale bar 25µm.

3.3. Electron microscopic observations

Measurement values are presented in table 1 and 2.

3.3.1. Maturation of parvalbumin-immunoreactive somata within dorsal layer II

At P10, four cells had nuclear envelopes with small indentations (figure 7A), and one cell had no nuclear indentation. All cells had nuclei that contained one to three nucleoli per thin section, and reaction deposit within their nuclei. When density of the reaction product was

compared within the cytoplasm and the nucleus, the reaction product was denser in the cytoplasm for two cells whereas the opposite was true for the remaining three cells.
The reaction product was homogeneously distributed in the cytoplasm for all cells. Somatic organelles included rough and smooth endoplasmic reticulum (ER), Golgi complex, multivesicular bodies and mitochondria.

Compared to P10, somata at P15 had deeper nuclear indentations. In the case of the two cell bodies with a visible nucleus, the nuclei contained non or two nucleoli per thin section and reaction product was distributed homogenously within the cytoplasm of all somata. One out of the two cells exhibited reaction product in the nuclei, and the reaction product was denser in the cytoplasm compared to the nucleus. The various types of organelles were the same as for P10, but with the addition of lysosomes (figure 7B). On average, cell bodies at P15 had the highest number and density of somatic mitochondria (table 1).

Compared to P15, somata at P30 had even deeper nuclear indentations (figure 7C), and increased number and density of lysosomes (table 1). The size of the lysosomes appeared larger than at P15. Two cells had a visible nucleus. In the individual nuclei, nucleoli varied in abundance from zero to three per thin section. The reaction product was denser in the nucleus compared with the karyoplasm for one of the cells. The number and density of somatic mitochondria were comparable to that of P10 (table 1).

Table 1: Overview of the measurements from P10, P15 and P30 somata.

Measurements		**P10**	**P15**	**P30**
Number of mitochondria per somata per thin section	Range	11 - 91	40 - 108	31 - 105
	Mean	50	72	54
	N	43	43	42
Mitochondria density (per μm^2 cytoplasm) per somata per thin section	Range	0.3 – 0.6	0.5 - 2	0.2 – 0.8
	Mean	0.5	1.1	0.4
	N	43	43	42
Number of lysosomes per somata per thin section	Range	0	0 - 9	0 - 15
	Mean	0	2.3	5.6
	N	43	43	42
Lysosome density (per μm^2 cytoplasm) per somata per thin section: lysosome	Range	0	0 – 0.22	0 – 0.12
	Mean	0	0.03	0.04
	N	43	43	42

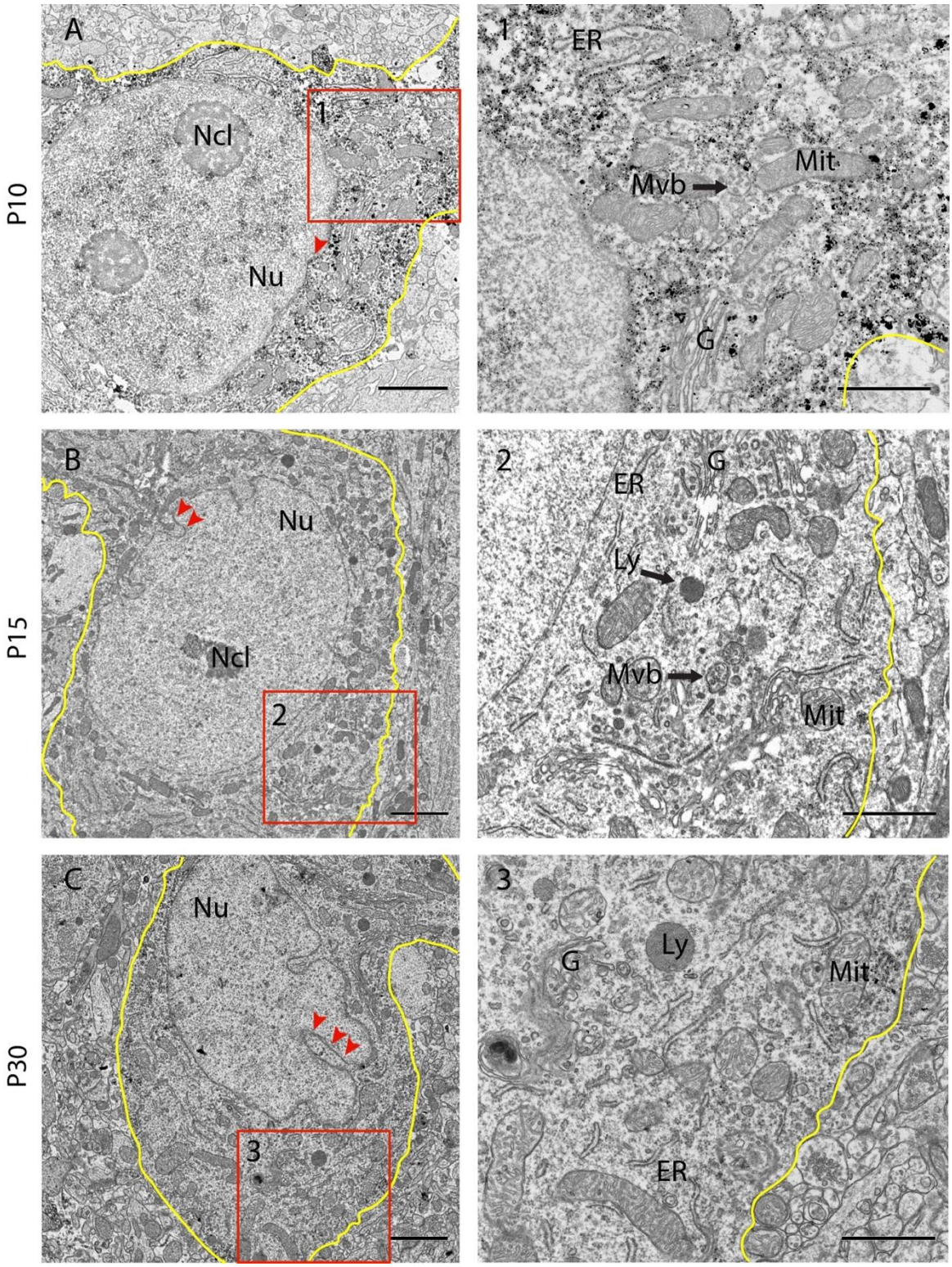

Figure 7: Electron micrographs illustrating PV+ somata at different developmental stages. (A) At P10, the nucleus (Nu) have small indentations (arrows), and contain nucleoli (Ncl), mitochondria (Mit), the endoplasmic reticulum (ER), multivesicular bodies (Mvb) and Golgi apparatus (G). At (B) P15 and (C) P30, the nuclear indentations are increasingly deeper and lysosomes (Ly) are present. The edges of the somata are colored for better visualization. Scale bar 5μm (A; B; C) and 1um (box 1; 2; 3).

3.3.2. Afferent innervation of parvalbumin-immunoreactive somata in dorsal layer II

All cell bodies were densely covered by both PV+ and immunonegative presynaptic terminals forming synaptic contact. All PV+ terminals were identified as symmetrical due to a lack of postsynaptic densities (PSDs) in the postsynaptic membrane. The average of the total number of axon terminals (PV+ and immunonegative) and terminal density were strikingly similar between each age group (table 2).

At P10, both PV+ and immunonegative axon terminals contained few and scattered vesicles. The majority of the presynaptic vesicles were round, and ellipsoid vesicles appeared less frequent at this point in time. Only a sparse number of potential immunonegative asymmetrical synapses were identified on the basis of potential PSDs in the postsynaptic membrane (figure 8A), which gave the majority of the immunonegative synapses a symmetrical appearance (figure 8D). The majority of both PV+ and immunonegative axon terminals displayed a round shape, while a small number were mushroom shaped. Two of the cell bodies were apposed by immunonegative *en passant* axon terminals. Four of the somata were innervated by PV+ terminals (figure X8). The number of different PV+ terminals that innervated each cell varied from 0 to 6 (figure 8). On average, each soma was contacted by one PV+ axon terminal per thin section (table 2). One third of the PV+ axon terminals (N = 5/17) contained mitochondria; one mitochondria per terminal per each thin section.

Compared to P10, presynaptic vesicles appeared more numerous at P15, and they were more often accumulated near the presynaptic site. Ellipsoid vesicles appeared more frequently. The postsynaptic membrane exhibited prominent PSDs (figure 8), such that both symmetrical and asymmetrical synapses were easier to separate than at P10. Lastly, whereas most terminals displayed a round shape at P10, most axon terminals displayed a mushroom shape or *en passant* at P15. All somata were innervated by immunonegative *en passant* terminals, and two of the somata were also innervated by two PV+ *en passant* axon terminals each. In one case, one PV+ axon terminal was connected to an adjacent PV+ terminals (figure 8J). All somata were innervated by PV+ terminals, and the average PV+ terminal density was higher than at P10. The number of different PV+ terminals innervating each soma were also higher than P10, and ranged from 5 to 19. On average, each soma was contacted by three PV+ axon terminal per thin section (table 2). The area of the PV+ terminals appeared smaller than for P10 (table 2). About half of the PV+ axon terminals (N = 21/46) contained mitochondria; one or two mitochondria per terminal per thin section. The area of mitochondria within the

PV+ axon terminals appeared larger at P15 compared to that of P10 (table 2). The mitochondria appeared less developed at P10 and P15 in terms of cristae.

With respect to terminal shape, presynaptic vesicles and PSDs, axon terminals at P30 appeared relatively similar to that of P15. Four cells were innervated by immunonegative *en passant* terminals, and one cell were additionally innervated by PV+ *en passant* terminals. All somata were innervated by PV+ terminals, and the average PV+ terminal density was lower than P15 but higher than P10. The number of different PV+ terminals that innervated each cell ranged from 1 to 17. On average, each soma was contacted by two PV+ axon terminal per thin section (table 2). The mean area of the PV+ terminals appeared larger than P10 and P15 (table 2). About half of the PV+ axon terminals (N = 18/35) contained mitochondria; one or two per thin section. The area of mitochondria within the PV+ axon terminals appeared largest at P30 (table 2), and the cristae appeared more mature.

Table 2: Overview of the measurements on afferent innervation at P10, P15 and P30.

Measurements		**P10**	**P15**	**P30**
Area of mitochondria per PV+ terminal per thin section (μm^2)	Range	0.2 – 0.7	0.1 – 2.5	0.2 – 3.7
	Mean	0.4	0.7	1.7
	N	9	58	58
Number of total axon terminals per somata per thin section	Range	14-29	14-40	15-40
	Mean	22	22	23
	N	43	43	42
Density of total axon terminals (per µm membrane) per somata per thin section	Range	0.2 – 0.6	0.2 – 0.6	0.2 – 0.5
	Mean	0.4	0.4	0.4
	N	43	43	42
Number of PV+ terminals per somata per thin section	Range	0 - 4	0 - 8	0 - 9
	Mean	1	3.1	2.3
	N	43	43	42
Density of PV+ terminals (per µm membrane) per somata per thin section	Range	0.01 – 0.06	0.02 – 0.1	0.01 – 0.1
	Mean	0.02	0.06	0.03
	N	43	43	42
Area of PV+ terminal per somata per thin section (μm^2)	Range	0.3 - 10	0.5 - 10	0.08 - 12
	Mean	4.2	3.0	5.4
	N	45	137	57

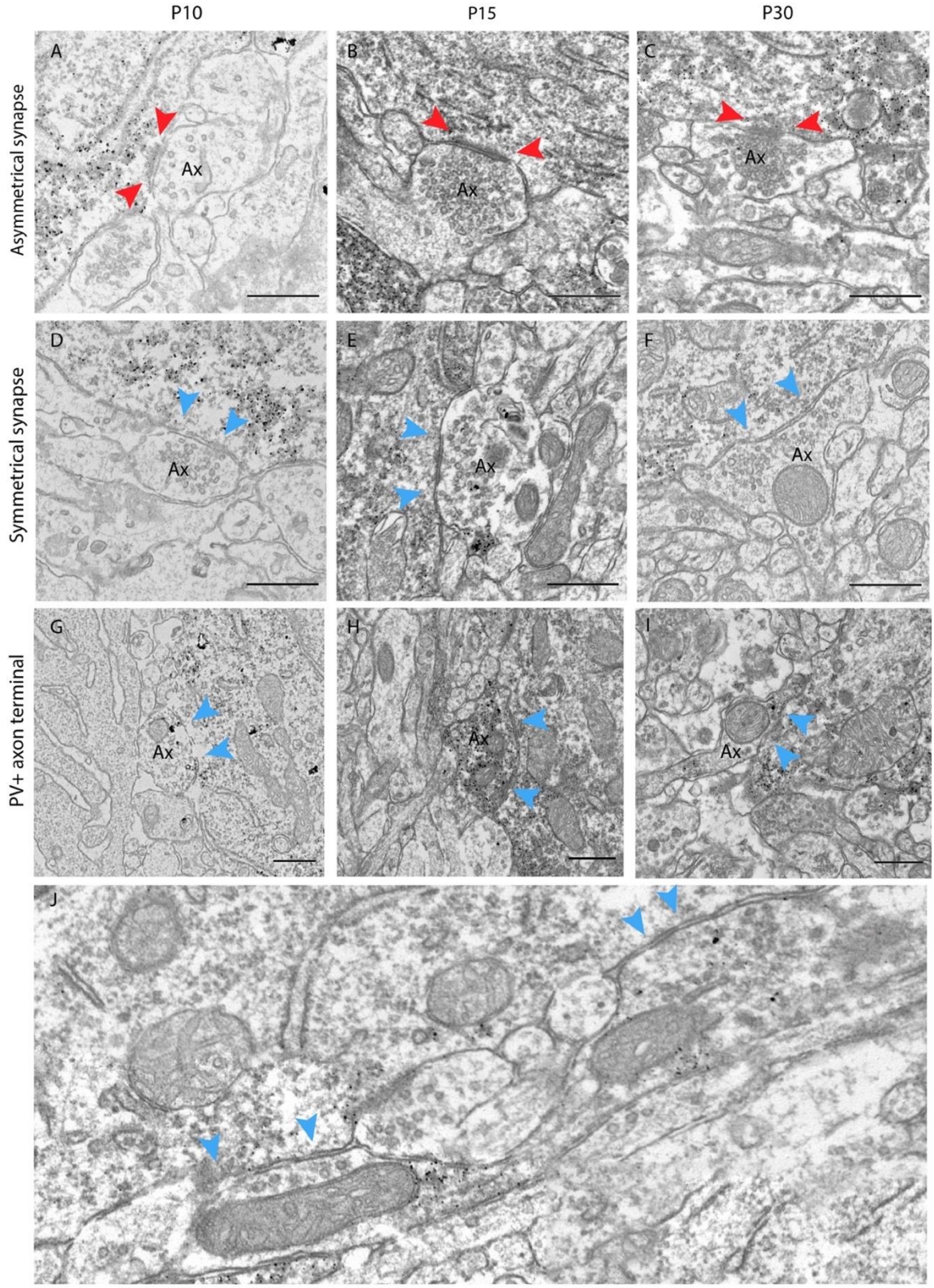

Figure 8: Electron micrographs illustrating axon terminals (Ax) innervating of PV+ somata within layer II in the developing rat MEC. Immunonegative terminal with asymmetrical synapse (red arrows) at (A) P10, (B) P15 and (C) P30. Immunonegative terminal with symmetrical synapse (blue arrows) at (D) P10, (E) P15 and (F) P30. PV+ terminal at (G) P10, (H) P15 and (I) P30. (J) Connected PV+ terminals at P15. Scale bar 500nm.

3.3.3. Additional observations from the perisomatic region within dorsal layer II

All somata displayed somatic spines, that took the form of a small finger-like protrusion on the otherwise smooth surface of the membrane. The number of different somatic spines per cell ranged from 1 to 5 (mean 2.5) at P10, 2 to 4 (mean 2.8) at P15 and 1 to 3 (mean 1.6) at P30. For all age groups, between non and two somatic spines were observed per somata per thin section. The somatic spines appeared devoid of major organelles, and these made synaptic contact with immunonegative terminals (figure 9). The somatic spines appeared largest at P10, and about half (N = 5/12) exhibited a mushroom-like appearance at P10. No somatic spines were found to make contact with PV+ terminals.

Proximal dendrites, axon initial segment and somatic spines were densely covered by immunonegative presynaptic terminals observed to make synaptic contact. All dendrites and axon initial segments made symmetric synapses with immunonegative terminals, whereas immunonegative asymmetrical synapses could be observed at P15 and P30. Proximal dendrites were frequently innervated by PV+ terminals at all ages, whereas only one axon initial segment were observed innervated by a PV+ terminal at P30 (figure 10). The morphology of both PV+ and immunonegative terminals innervating these regions were comparable to the somatic innervation already described in section 3.3.2.

For all age groups, the dendrites appeared to vary in size and their diameter both increased and decreased along their course. At all ages, the most prominent organelles within the dendritic cytoplasm were multivesicular bodies, endoplasmic reticulum and mitochondria oriented longitudinally to the dendritic membrane. Whereas no microtubules could be identified at P10, microtubules were one of the most prominent dendritic features at P15 and P30.

The axonal initial segment was identifiable by the electron dense layer of material beneath the plasma membrane and by the fasciculation of microtubules (figure 10). Neither this layer nor microtubules were identifiable at P10, and the following description is based on axons radiating out from somata at P15 and P30. The axons had smooth and spine-less contours and displayed a fairly uniform shape once they have passed the gradually narrowing initial segment. Microtubules appeared to form modest fascicles in the axonal initial segment. Lysosomes, ER and mitochondria oriented longitudinally to the axonal membrane were also present.

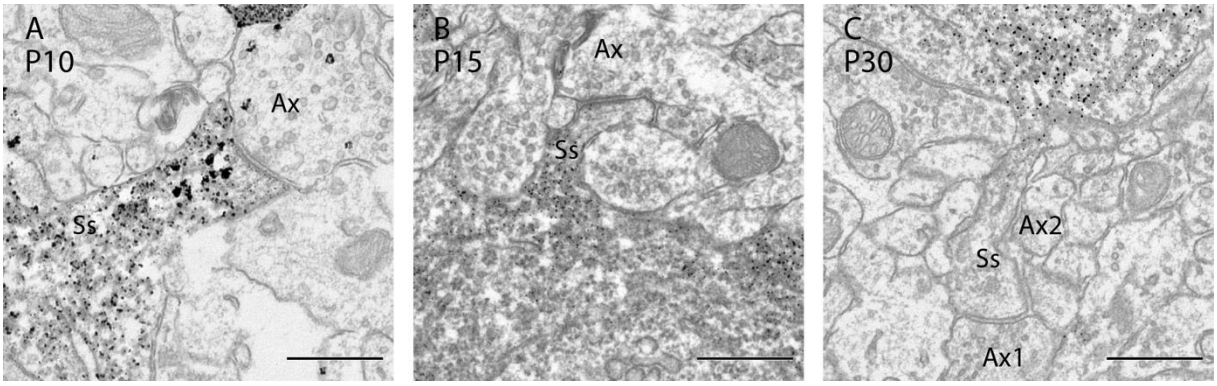

Figure 9: Electron micrographs illustrating somatic spines (Ss) on PV+ somata innervated by immunonegative axon terminals (Ax) at (A) P10, (B) P15 and (C) P30. Scale bar 500nm

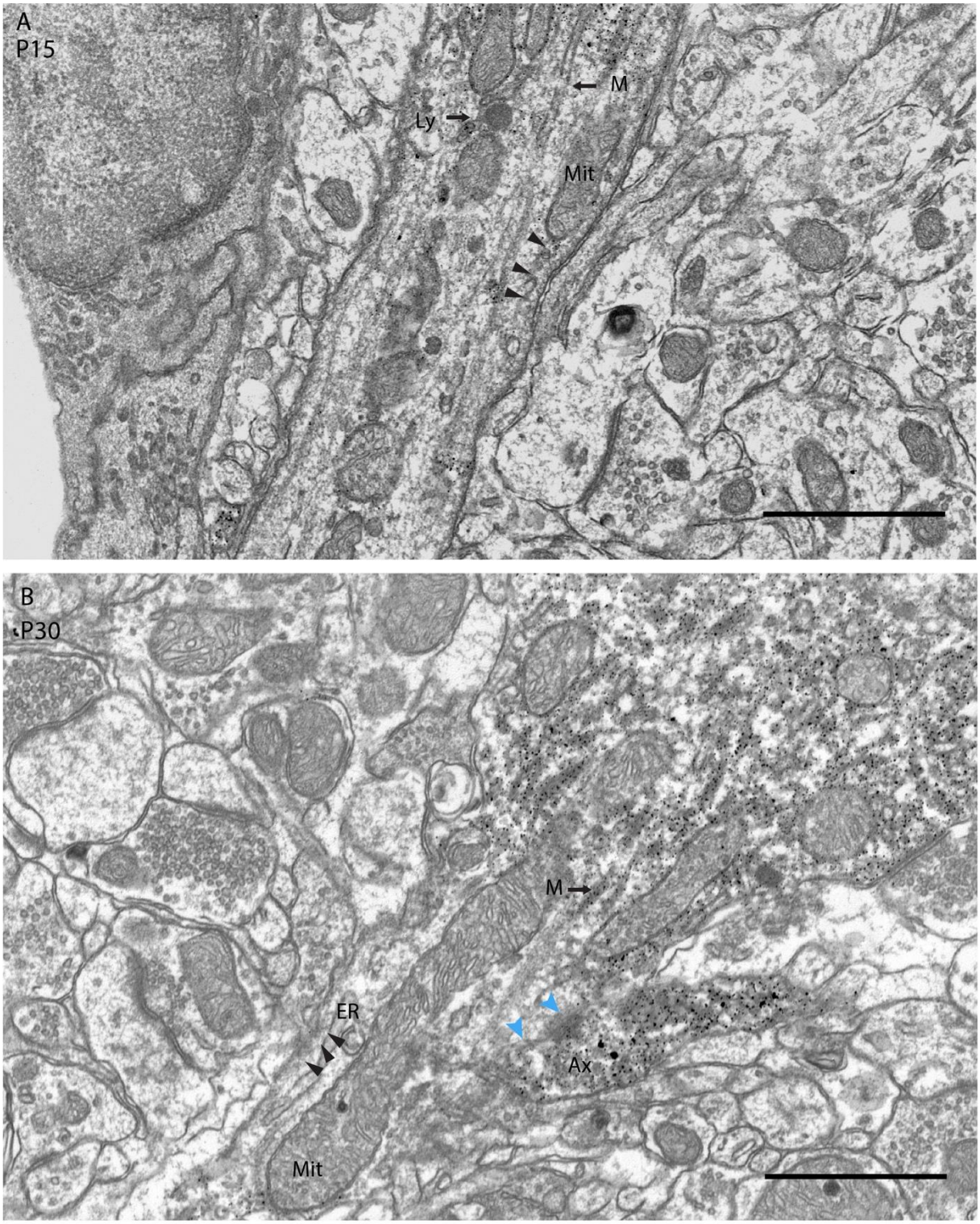

Figure 10: Electron micrographs illustrating the axonal initial segment of PV+ somata at (A) P15 and (B) P30, and the innervation of a PV+ axon terminal (blue arrows). The axon initial segments were characterized by a dense undercoating of the plasma membrane (black arrows), and contained microtubules (M), mitochondria (Mit), ER and lysosomes (Ly). Scale bar 1μm.

4. Discussion

4.1. Parvalbumin expression within the developing medial entorhinal cortex

Postnatal maturation of PV+ cells within the rat MEC was investigated by use of immunohistochemistry and LM. Five male rats at P10 (N = 1), P15 (N = 2) and P30 (N = 2) were subject for analysis, each represented by two sagittal vibratome sections.

1.4.1. Expression at postnatal day 10 and laminar specificity

One of the major findings from use of LM is that PV was expressed within the rat MEC at P10. Since PV+ somata and dendrites were most densely labeled within the superficial layers, and few PV+ somata and dendrites could be observed in layer V/VI, PV might be expressed according to a laminar specificity. Spars labeling within layer V/VI could indicate that few cells are present within the deep layer at P10. Alternatively, it might reflect an immature synthesis of the PV protein. Because PV is distributed within the entire somatic and dendritic cytoplasm (Nitsch et al. 1990), sparse labeling within layer V/VI may indicate that these cells had just started to express PV at P10. Laminar specificity in PV expression might indicate that cells within the superficial layers mature before cells in the deeper layers, and could potentially result from the connectional differences between the superficial- and deep layers of the MEC (Canto et al. 2008).

This finding is contrary to studies of the rat cerebral cortex, where PV is first expressed within the deeper layers (Alcántara et al. 1993). Although one cannot draw conclusions about which layer of the MEC PV is expressed first from this study, distribution of PV within dendritic cytoplasm indicates that PV cells within the superficial layers mature before PV cells in the deep layers of the MEC. These differences might reflect general differences between the evolutionary ‘old’ EC and the ‘new’ neocortex in rats.

The pattern of laminar specificity presented in this thesis is also somewhat different to the primate MEC, where PV expression first appear within layer III in humans (Grateron et al. 2003) and layer III and V in monkeys (Berger et al. 1993; Grateron et al. 2003). These differences might indicate general differences between PV+ cells in the rodent and primate MEC.

1.4.2. Dorso-ventral gradient within layer I

Observations from the LM experiment indicated that PV expression within layer I decrease from dorsal to ventral at P10. This could be the result of poor antibody penetration in the ventral part of the section. Alternatively, it might relate to development of MEC network. This gradient of PV expression is similar to development of Calb+ neurons within the rat MEC, where calbindin is expressed in the dorsal layer II before the ventral layer II (Ray & Brecht 2016), and might indicate that cells belonging to same microcircuitry mature at the same time. That is to say, mature in the dorsal part before the ventral part of the rat MEC.

A possible explanation for this trend during development could be that it is related to the grid cells within the MEC. Mature grid cells exhibit a dorsal-ventral gradient both in terms of their physiological activity (Stensola et al. 2012) and the amount of innervation from PV+ axon terminals (Beed et al. 2013). Although mature grid firing properties are first observed at P25 in the rat MEC (Langston et al. 2010), the dorso-ventral gradient observed in this thesis might be related to the wiring of the MEC microcircuitry and grid cell development.

No dorso-ventral gradient were observed in layer I at P15 or P30, which most likely result from the generall increase in PV+ dendrites observed at the time.

4.2. Parvalbumin-expressing somata and the afferents that innervate them within dorsal layer II

Postnatal maturation of PV+ cells within dorsal layer II of the rat MEC was investigated by use of immunohistochemistry, LM and EM. Four brains from male rats at P10 (N = 1), P15 (N = 1) and P30 (N = 2) were subject for analysis. P10 was represented by one vibratome sections, whereas P15 and P30 were represented by two vibratome sections per animal. Thin sections were obtained from tissue blocks containing the dorsal part of the MEC. For each age group, five PV+ cells were followed for eight to nine thin sections. The axon terminals that innervated the PV+ somata was examined in each thin section, and special attention was paid to the PV+ afferent.

4.2.1. Cell bodies

From looking at morphology and somatic ultrastructure, it appears that PV+ somata within dorsal layer II undergo several changes from P10 to P30.

Measures from the LM experiment indicated that the average size of the PV+ cell bodies increased most profoundly from P10 (long axis 16μm/short axis 11μm) to P15 (long

axis 19μm/short axis 12μm). This increase might be related to changes in specific membrane properties of the PV+ cells. Within the mouse DG, the area of basket cell bodies also increases from P10 to P15. Consistent with this increase is a decrease in input resistance and an increase in the membrane time constant, such that the time scale of the cells response to changes in somatic input increases (Doischer et al. 2008). This might indicate that the PV+ cells within layer II of the dorsal MEC become increasingly capable of intergrating synaptic input to their somata from P10 to P15. Changes in somata size, and potential membrane properties, would presumably be driven by changes in genetic transcription, and EM observation indicates that changes in gene expression takes place during this time period.

The EM experiment indicates that reaction product was more often found in the nuclei of cells at P10 (N = 5) than at P15 (N = 1) or P30 (N = 2), and only at P10 were the reaction product found to be denser within the nuclei than the cytoplasm. This indicates that there might be a decrease in nuclear reaction product during development. Although the DAB reaction product did not necessarily reflect the distribution of the antigen, as a diffusion of the reaction may occur (Novikoff et al. 1972), the finding that about half of the cells shows reaction product in the nuclei at P15 and P30 is similar to what have been described in the adult MEC (Wouterlood et al. 1995). Within the mouse HF, nuclear PV signals have been found to control the structural features of neurons (Mauceri et al. 2015), and increased levels of nuclear PV were linked to altered expression of genes that regulate neuronal architecture. On the basis of the latter study, there might be a shift in gene transcription of the PV+ cells from P10 to P15, such that gene transcription with following changes in cell structure are more expressed at P10 than at P15. Complementary to this line of thoughts is the changes in dendritic architecture and cellular shape observed at both the LM- and EM-level from P10 to P15.

EM observations also indicated that the PV+ somata had increasingly deeper nuclear indentations through development. This finding is similar to development of basket cells in the rat DG (Seress & Ribak, 1990), and resembles features described for PV+ cells within the adult rat MEC (Wouterlood et al. 1995). Nuclear geometry have been related to nuclear calcium signaling, and nuclei with infoldings will allow for a much more precise calcium signaling than spherical nuclei (Wittmann et al. 2009). The change in the nuclear geometry observed in this study might indicate that the PV+ cells within layer II of the dorsal MEC are less sensitive to individual calcium signals at P10 compared to P15 and P30 where nuclear indentations are deeper. Because nuclear calcium functions as a signal integrator in synapse-

to-nucleus communication (Bading 2013), increased sensitivity to calcium signals would enhance activity-based transcriptional activity within the PV+ cells from P10 to P30. Interestingly, it has been shown that the geometry of the nucleus can undergo synaptic activity-dependent changes, and that burst activity resulted in increased nuclear indentations (Wittmann et al. 2009). Thus, the changes in nuclear shape observed in this study from P10 to P30 could be explained by increased functionality of the synaptic innervation of the PV+ cells during this time period.

Observations from the EM experiment further indicated that all cell bodies exhibited somatic spines, but the average number of somatic spines per somata was higher at P10 (N = 2.5) and P15 (*N* = 2.8) compared to P30 (*N* = 1.6). While somatic spines are not described in the adult MEC (Soriano et al. 1993; Wouterlood et al. 1995), Bundman and colleagues (1994) have reported that granule cells within the adult rat DG exhibited an increased number and size of somatic spines following induced seizures. Because seizures results from unbalance between excitation and inhibition (Yekhlef et al. 2015), the increased frequency of somatic spines observed at P10 and P15 in this study, might indicate that the cells are subject for enhanced excitation during this time period. Enhanced excitation at P10 and P15 could be explained by the shift in synaptic activity observed in the rat around P15, such that GABA is depolarizing up to this point (Ben-Ari 2001). A shift in synaptic activity around P15 would restore the balance between excitation and inhibition, and might explain the reduction of somatic spines from P15 to P30. While knowledge on the function of somatic spines is incomplete, the present thesis found that the somatic spines were innervated by immunonegative axon terminals, which might indicate that the somatic spines provides a larger surface area to excite the cells at P10 and P15.

Observations from the EM also indicated that lysosomes were not present at P10, and their number increased from P15 to P30. Lysosomes play an important role in the degradation of a variety of old or potential harmful intracellular substrates (Carmona-Gutierrez et al. 2016), and the steady increase in lysosomes likely indicates increased activity of cytoplasmic organelles. It could also be related to the formation of new synapses. Autophagy, a major determinant of protein turnover, is essential during formation of new synapses. It operates by sequencing cytoplasmic material into autophagosomes, which is subsequently transported to the cell soma where it fuses with lysosomes (Shen et al. 2015). Studies of cultured hippocampal neurons have shown that autophagy is required both during synapse formation (Petralia et al. 2013), and synapse elimination (G. Tang et al. 2014; Bowling & Klann 2014).

Thus, the presence of lysosomes observed in the PV+ somata at P15 could be related to formation of new connections within the MEC, and is complementary to the changes in PV+ axon terminals observed from P10 to P30.

Finally, the average number and density of somatic mitochondria were higher at P15 (72/1.1) compared to that of P10 (50/0.5) and P30 (54/0.4). Since mitochondria are responsible for generating energy (Chan 2006), this finding indicate that energy demands might be higher at P15 than P10 and P30, and might be related to the functional onset of the cells. Within the mouse barrel cortex, fast-spiking cells have been found to express mature firing patterns around P15, including discharge of sustained trains of action potentials at high frequency in response to sustained depolarization (Goldberg et al. 2011). The increased number and density of mitochondria observed in this study at P15 might thus be related to functional onset of the PV+ cells. Although the identity of the PV+ axon terminals were not be determined in the present thesis, the average number of PV+ axon terminals was indeed highest at P15 and their appearance looked mature at P15, which might support the notion that the PV+ cells are more active and require more energy at this point in time.

4.2.2. Axon terminals

4.2.2.1. Maturation of immunopositive and immunonegative axon terminals

From looking at ultrastructure of axon terminals innervation the PV+ somata within dorsal layer II of the rat MEC, it appears that the recruitment of PV+ cells through somatic innervation undergo several changes from P10 to P30. This section will not separate between PV+ and immunonegative terminals unless otherwise specified.

EM observations indicated that the PV+ cell bodies contained a sparse number of potential PSDs at P10, which made most synapses appear symmetrical and thus inhibitory. This indicates that the inhibitory axon terminal that innervate PV+ somata within dorsal layer II of the rat MEC might mature before the excitatory axon terminals. Developmental differences in somatic innervation can most likely be explained by the GABA-switch. GABA is initially excitatory as a consequence of high intracellular concentration of chloride (Ben-Ari et al. 1989), and activation of inhibitory afferent will result in depolarization of the PV+ cell. Inhibitory afferents may therefore mature earlier than excitatory afferents, because there is no need for hyperpolarization of the PV+ cell while the excitatory synapses are immature. Indeed, inhibitory synapses have been found to mature before excitatory synapses in the rat

CA1 (Tyzio et al. 1999). It should be noted that neither the excitatory nor inhibitory input appeared fully mature at this point in time. Additional EM observations indicated that PV+ somata were innervated by axon terminals that contained few and scattered vesicles at P10. Hence, the synapses lacked several of the morphological features characterizing mature synapses at P10 (Colonnier 1968), and might be less active at this point in time because presynaptic properties such as vesicle release are partly determined by the availability of vesicles for release (Mozhayeva et al. 2002). It has been shown that presynaptic terminals that lack readily releasable vesicles may release neurotransmitters during strong stimulation (Mozhayeva et al. 2002). Thus, the sparse number of presynaptic vesicles observed in this study at P10 might indicate that the terminals are less active at P10 compared to P15 and P30. Albeit only measured in the PV+ axon terminals, the sparse number and size of terminal mitochondria indicate that the axon terminals have smaller energy requirements at P10 than at P15. Taken together, the ultrastructure of the axon terminals indicate that strong stimulation is probably required to stimulate transmitter release from the at P10, and would most likely depolarize the PV+ somata at this point in time.

EM observations from P15 indicated that the axon terminals contained an increased number of pleomorphic vesicles, clustered near the active zone. This is similar to features that characterize mature synapses (Colonnier 1968), and indicates that there is an increased availability of vesicles for release (Mozhayeva et al. 2002). Parallel to maturation of the synapse is an increased number and size of mitochondria within the PV+ axon terminals, indicating that the energy requirements increase within the presynaptic terminals from P10 to P15. This observation is in line with maturation of fast-spiking cells within the mouse barrel cortex, who show mature activity patterns around P15 (Goldberg et al. 2011). Parallel to changes within the terminal cytosol, are changes in the architecture of the presynaptic terminals. Whereas two cell bodies at P10 was contacted by immunonegative *en passant* terminals at P10, all five somata were contacted by immunonegative *en passant* terminals at P15. Since a large number of *en passant* terminals may arise from the same axonal arbor, presynaptic vesicles will be released synchronously (Hu et al. 2014). This is more powerful than the asynchronous vesicle release of round and mushroom boutons (Hu et al. 2014). The increased number of *en passant* boutons indicate that the synaptic control of the PV+ somata are stronger at P15 than P10. It is interesting to note that these changes in morphology occur at a time when GABA is usually becoming hyperpolarizing. When there is an adequate density of GABAergic- and glutamatergic synapses, usually around P15, a chloride-extruding

system enables chloride to be pumped out from the intracellular matrix. As a consequence, GABAergic transmission become hyperpolarizing (Ben-Ari 2001). Taken together with the findings from the present thesis, the axon terminal appear more active and the synapse more mature at P15 than at P10. This occurs at a time when GABA become hyperpolarizing, indicating that the afferent innervation of the PV+ somata are more diverse at P15.

The axon terminals appeared relatively similar at P30 to that of P15, indicating that the major developmental changes likely take place between P10 and P15. However, there appeared to be an increase in the average number and size of mitochondria within the PV+ axon terminals, indicating increased energy requirements in the terminals from P15 to P30. Terminal mitochondria produce much of the energy required to maintain synaptic ion homeostasis, and is required for neurons to form and maintain functional synapses (Cheng et al. 2012). Time-lapse confocal microscopy have shown that a reduction of dendritic mitochondria lead to a loss of synapses and dendritic spines, whereas an increase in dendritic mitochondria lead to enhanced number and plasticity of spines and synapses (Li et al. 2004). Since there appears to be an association between mitochondrial number and the active period of synaptogenesis, the increased number and size of mitochondria observed in PV+ axon terminals from P15 to P30 is likely related to the maintenance, formation and reorganization of the afferent innervation of the PV+ somata from P15 to P30.

4.2.2.2. Overshoot and pruning of parvalbumin-expressing axon terminals

One of the findings from use of EM was that most PV+ somata within dorsal layer II of the rat MEC are innervated by both PV+ and immunonegative axonal terminals at P10. The average number and density of all axon terminals (PV+ and immunonegative) were strikingly similar at P10 (22/0.4), P15 (22/0.4) and P30 (23/0.4). However, when separating between PV+ and immunonegative afferents, PV+ innervation appeared to change after P10. The average number and density of the PV+ axon terminals increased from P10 (1/0.02) to P15 (3.1/0.06), and decreased from P15 to P30 (2.3/0.03). This indicates that there is an overproduction of PV+ axon terminals early in postnatal life, followed by a period of pruning. A similar trend have been observed in PV+ input to immunonegative somata within dorsal layer II of the rat MEC (Bjerke 2016), in the rat cerebral cortex (Dyson & Jones 1980), and in the electrical coupling between PV+ basket cells within the mouse DG (Meyer et al. 2002), and indicates that it is in accordance with normal development.

Whereas the number of PV+ axon terminals increased, their size appeared decreased from P10 to P15. This is similar to what have been found on PV+ axon terminals innervating immunonegative somata in dorsal layer II of the rat MEC (Bjerke 2016) and rat cerebral cortex (Armstrong-James & Johnson 1970). The latter study explained this finding by arguing that during the phase of rapid expansion in number of synapses, the newly formed synapses are smaller. The overproduction of PV+ axon terminals is interesting in the light of a study by Sail and Drake-Baumann (1994), who found that blockage of all electric activity in cerebellar cultures for two weeks resulted in reduced inhibitory synaptogenesis. The number of inhibitory synapses on the Purkinje cell somata was reduced to about half of the control value. Interestingly, there were no loss of excitatory synapses on the Purkinje cell dendrites (Seil & Drake-Baumann 1994). This study indicates that synaptogenesis of inhibitory input are activity-driven, and increased number and density of the PV+ axon terminals may be important for the wiring of the spatial network within the MEC. At P10, rats responds to olfactory stimulation, stay within the nest, crawl instead of walk and their eyes are closed (Wills et al. 2014). This indicates that sensory input and experience with the surrounding environment is limited in P10 rats. At P15, rats have opened their eyes, walk properly and starts to move into open fields (Wills et al. 2014), indicating that their sensory input is more diverse than at P10. Since exploration of novel environment is dependent on the HF (Morris et al. 1982), the development of sensory, motor and spatial behavior might result in an overproduction of PV+ axon terminals at P15.

EM observations indicated that an overshoot of PV+ axon terminals at P15 is followed by a period of pruning. Similar to the increase of axon terminals, synaptic pruning appear also to be depended on neuronal activity (Gabriele et al. 2000; Sanes & Takács 1993). The present thesis indicated that the size of the PV+ axon terminals were larger at P30 than at P15. Similar results have been found in the rat somatosensory cortex (Dufour et al. 2016; Dyson & Jones 1980), where the increase of presynaptic terminal area was was correlated with an increase in the length of the synaptic junction in the postsynaptic terminal, which indicated increased functionality (Dyson & Jones 1980). As previously mentioned, P15 is the time when fast-spiking basket cells begin to express mature firing patterns (Goldberg et al. 2011), which indicates that the pruning observed between P15 and P30 may be activity-driven. Several changes occur in the rat from P15 to P30; primary visual neurons responds to visual stimuli, they leave the nest to explore surroundings and they can be trained to locate the platform in the Morris water maze task (Wills et al. 2014). Given the involvement of PV+

cells in spatial navigation (Buetfering et al. 2014; Beed et al. 2013; Gonzalez-Sulser et al. 2014), experience from increased visual input and exploration of the surrounding environment might refine the PV+ axonal innervation of the PV+ somata and optimize the interconnectivity between the PV+ cells.

4.2.2.3. Differences in parvalbumin innervation within age groups

Based on the average measures from P10, P15 and P30, the present thesis indicates that there were an overshoot and refinement of PV+ axon terminals during this time period. However, it should be noted that there were large variations in the number and density of the PV+ axon terminals within each age group. Several explanations can account for these differences in PV+ innervation.

First, three types of PV+ cells have been identified within layer II of the rat MEC; horizontal chandelier-, vertical chandelier- and basket cells (Canto et al. 2008). Because the present study could not separate between these cell types, the observed differences in PV+ innervation within each age groups may reflect differences in connectivity between these cell types.

Second, differences in PV+ innervation could be related to subgroups of the PV+ basket cells. A recent study by Donato and colleagues (2015) showed that PV+ basket cells within the mouse CA1 consists of two subpopulations defined by their scheduled neurogenesis. These subgroups exhibited distinct input connectivity, output target neurons and roles in learning. Learning that relied on rule application induced alterations in excitatory afferents onto the 'early-born' PV+ basket cells, whereas 'late-born' PV+ basket cells were unaffected. Learning that depended on enhanced acquisition and combination of new information on the other hand, induced alterations in inhibitory afferents onto 'late-born' PV+ basket cells and did not affect the 'early-born' PV+ basket cells. Interestingly, the 'late-born' cells were specifically involved in regulation of plasticity during critical periods of postnatal development (Donato et al. 2015). If similar subpopulations of PV+ basket cells exist within layer II of the MEC, their afferent innervation would be altered on the basis of their recruitment, and could explain the large variety of PV+ afferent connectivity observed within each age group in this study.

Finally, Armstrong and colleagues (2015) recently showed that individual PV+ basket cells varied in terms of the proportion of boutons innervating Calb+ and reelin+ cells within layer II of the MEC. This indicated that the PV+ basket cells were selective for principal cell types with respect to their divergent output of the MEC, and that PV-derived inhibition is not

a homogenous ‘blanket’ of inhibition as previously suggested for neocortical networks (Packer & Yuste 2011). The result from the present study support the notion about PV+ target-selectivity proposed by by Armstrong and colleagues (2015), and suggest that PV+ cells within layer II have a preference on the postsynaptic target, not only in terms of principal cells, but also in terms of PV+ cells. This indicates that the PV+ network might be more intricate than previously thought.

4.3. Future directions

The present thesis indicates that there are developmental changes in MEC PV+ cells within and the axon terminals that innervate their somata. These results should be replicated in additional studies with a larger sample size for further verification, but also include identification of presynaptic target cells. First, immunohistochemical studies with double-labeling for EM can address questions regarding the identity of the immunonegative axon terminals. With the finding of immunonegative *en passant* terminals on the PV+ somata in mind, the possibility that the PV+ somata are innervated by another type of MEC basket cell should be addressed. Second, 3D-EM can provide more detailed information regarding the size and the shape of axon terminals and somata of MEC neurons during development. Third, future EM experiments should explore properties of PV+ cells and their interconnectivity along the entire dorso-ventral axis of MEC. Fourth, while no other types of microscope can provide better magnification than EM, it cannot provide a complete picture of connectivity between the PV+ cells population within the MEC. Other microscope types such as confocal microscopy with immunofluorescence antibodies, should be used in combination with EM to shed light on the interconnectivity between PV+ cells within layer II of the MEC.

The present thesis also indicated that PV+ cells within superficial layers may mature before PV+ cells in the deep layers of the MEC. The specificity of PV expression should be addressed by use of EM and immunohistochemistry for PV in deeper layers of the MEC.

4.4. Methodological considerations

Several issues with the methods used in the present thesis need to be considered, as they may have influenced the analysis of the results.

The brains used for the analysis were subject to somewhat different immunohistochemical treatments. Due to age-specific requirements, P10 rats subjected for EM were treated in a separate experiment and under different conditions than P15 and P30.

The major difference in this respect was the absence or use of Tx-100 in the pre-incubation step, which affected the penetration of the antibody and / or the visibility of the cellular membranes. Although antibodies might penetrate P10 more easily, the different treatments may have influenced the number of PV+ axon terminals seen in the respective age groups.

A second issue is the sample size. Each age group were initially represented by two brains, but poor morphology and a lack of immunoreactivity resulted in that both P10 and P15 were only represented by one brain. Although the adequate sample size within qualitative research is relative, a sample size of one per each group is not sufficient to permit generalization of the findings. Thus, a larger number of rats should be included in future studies.

Another issue worth considering, is the fact that the grid firing pattern and PV+ axonal innervation varies within layer II of the MEC (Stensola et al. 2012; Beed et al. 2013), and it was important to sample cells within the same region of the MEC to compare different sections. To accomplish this, selection of vibratome sections was largely based on the shape of the HF. However, the possibility that some of the areas of the MEC are more medial than others cannot be excluded, and might have had an influence on the final results. However, the largest variation reported in relation to connectivity is along the dorso-ventral axis (Beed et al. 2013), and all sections subject for EM was taken from the dorsal part.

Several problems with immunohistochemistry should also be considered. First, immunohistochemical procedures may change cellular morphology, especially via shrinking of the tissue, which may result from prolonged exposure to fixatives (Howat & Wilson 2014). One of the P30 brains was exposed to the fixative for several weeks longer than the other brains, which might have interfered with the analysis of the results. Second, cellular membranes were sectioned at random depths, which might have impacted on the visualization of individual synapses and could therefore have hampered the identification and classification of terminals. Third, PV penetration was poor in the sections used for EM, and PV labeling decreased after 4 to 5µm into the tissue block. This might have influenced the identification of PV+ axon terminals, and thus the classification and number of PV+ terminals. Fourth, due to extensive labeling with DAB, it was sometimes difficult to determine whether a synapse was symmetrical or asymmetrical, and might have interfered with the categorization of the various terminals.

5. Conclusion

The present thesis has investigated the maturation of PV+ cells within the rat MEC at P10, P15 and P30 by use of immunohistochemistry, LM and EM. Special attention was paid to PV+ cell bodies within dorsal layer II, and the axonal terminals innervating them. The results showed that PV were expressed within the MEC at P10, but the expression was especially dense in layer II and appeared to follow a dorso-ventral gradient in layer I. At P10, PV+ somata within dorsal layer II appeared immature, with small nuclear indentations and somatic spines, and were contacted by immature-looking PV+ and immunonegative axon terminals. Changes in the nuclear shape, somatic spines, number and location of presynaptic vesicles, shape of the axon terminals, PSDs and terminal mitochondria from P10 to P30, indicated that maturation of PV+ somata and the axons innervating them extended several weeks into the postnatal period. The average number of PV+ axon terminals were observed to overshoot, followed by a period of pruning. Finally, large variations in the number of PV+ axon terminals within each age group indicated that the interconnectivity between MEC PV+ cells may be more intricate than previously thought.

6. References

Alcántara, S., Ferrer, I. & Soriano, E., 1993. Postnatal development of parvalbumin and calbindin D28K immunoreactivities in the cerebral cortex of the rat. *Anatomy and embryology*, 188(1), pp.63–73.

Armstrong-James, M. & Johnson, R., 1970. Quantitative studies of postnatal changes in synapses in rat superficial motor cerebral cortex. An electron microscopical study. *Zeitschrift für Zellforschung und mikroskopische Anatomie (Vienna, Austria : 1948)*, 110(4), pp.559–68.

Armstrong, C. et al., 2015. Target-Selectivity of Parvalbumin-Positive Interneurons in Layer II of Medial Entorhinal Cortex in Normal and Epileptic Animals. *Hippocampus*, 26(6), pp.779–793.

Ascoli, G.A. et al., 2008. Petilla terminology: nomenclature of features of GABAergic interneurons of the cerebral cortex. *Nature Reviews Neuroscience*, 9(7), pp.557–568.

Bacci, A., Huguenard, J.R. & Prince, D.A., 2003. Functional autaptic neurotransmission in fast-spiking interneurons: a novel form of feedback inhibition in the neocortex. *The Journal of neuroscience : the official journal of the Society for Neuroscience*, 23(3), pp.859–66.

Bading, H., 2013. Nuclear calcium signalling in the regulation of brain function. *Nature reviews. Neuroscience*, 14(9), pp.593–608.

Bartos, M. et al., 2001. Rapid signaling at inhibitory synapses in a dentate gyrus interneuron network. *The Journal of neuroscience : the official journal of the Society for Neuroscience*, 21(8), pp.2687–98.

Bartos, M., Vida, I. & Jonas, P., 2007. Synaptic mechanisms of synchronized gamma oscillations in inhibitory interneuron networks. *Nature reviews. Neuroscience*, 8(1), pp.45–56.

Beed, P. et al., 2013. Inhibitory Gradient along the Dorsoventral Axis in the Medial Entorhinal Cortex. *Neuron*, 79(6), pp.1197–1207.

Ben-Ari, Y., 2001. Developing networks play a similar melody. *Trends in Neurosciences*, 24(6), pp.353–360.

Ben-Ari, Y. et al., 1989. Giant synaptic potentials in immature rat CA3 hippocampal neurones. *The Journal of physiology*, 416(1), pp.303–25.

Berger, B., Alvarez, C. & Goldman-Rakic, P.S., 1993. Neurochemical development of the hippocampal region in the fetal rhesus monkey. I. Early appearance of peptides, calcium-binding proteins, DARPP-32, and monoamine innervation in the entorhinal cortex during the first half of gestation (E47 to E90). *Hippocampus*, 3(3), pp.279–305.

Bjerke, I. 2016. Parvalbumin positive basket terminals in layer II of the rat medial entorhinal cortex: Postnatal developmed studied by immune-electron microscopy. Master´s Thesis.

Boccara, C.N. et al., 2015. A three-plane architectonic atlas of the rat hippocampal region. *Hippocampus*, 25(7), pp.838–857.

Boccara, C.N. et al., 2010. Grid cells in pre- and parasubiculum. *Nature neuroscience*, 13(8), pp.987–94.

Bowling, H. & Klann, E., 2014. Shaping dendritic spines in autism spectrum disorder: mTORC1-dependent macroautophagy. *Neuron*, 83(5), pp.994–6.

Buetfering, C., Allen, K. & Monyer, H., 2014. Parvalbumin interneurons provide grid cell–driven recurrent inhibition in the medial entorhinal cortex. *Nature Neuroscience*, 17(5), pp.710–718.

Buhl, E.H., Halasy, K. & Somogyi, P., 1994. Diverse sources of hippocampal unitary inhibitory postsynaptic potentials and the number of synaptic release sites. *Nature*,

368(6474), pp.823–8.
Bundman, M.C., Pico, R.M. & Gall, C.M., 1994. Ultrastructural plasticity of the dentate gyrus granule cells following recurrent limbic seizures: I. Increase in somatic spines. *Hippocampus*, 4(5), pp.601–10.
Burgalossi, A. et al., 2011. Microcircuits of functionally identified neurons in the rat medial entorhinal cortex. *Neuron*, 70(4), pp.773–86.
Buzsáki, G., 1984. Feed-forward inhibition in the hippocampal formation. *Progress in neurobiology*, 22(2), pp.131–53.
Buzsáki, G. & Draguhn, A., 2004. Neuronal oscillations in cortical networks. *Science (New York, N.Y.)*, 304(5679), pp.1926–9.
Canto, C.B. & Witter, M.P., 2012. Cellular properties of principal neurons in the rat entorhinal cortex. II. The medial entorhinal cortex. *Hippocampus*, 22(6), pp.1277–1299.
Canto, C.B., Wouterlood, F.G. & Witter, M.P., 2008. What Does the Anatomical Organization of the Entorhinal Cortex Tell Us? *Neural Plasticity*, 2008, pp.1–18.
Cappaert et al., 2014. 'Hippocampal formation' in G Paxinos, (eds), *The Rat Nervous system*, pp. 513-514.Academic Press, New York.
Carmona-Gutierrez, D. et al., 2016. The crucial impact of lysosomes in aging and longevity. *Ageing research reviews*. Available at: http://www.ncbi.nlm.nih.gov/pubmed/27125853 [Accessed May 4, 2016].
Chan, D.C., 2006. Mitochondria: dynamic organelles in disease, aging, and development. *Cell*, 125(7), pp.1241–52.
Cheng, A. et al., 2012. Involvement of PGC-1α in the formation and maintenance of neuronal dendritic spines. *Nature communications*, 3, p.1250.
Colonnier, M., 1968. Synaptic patterns on different cell types in the different laminae of the cat visual cortex. An electron microscope study. *Brain research*, 9(2), pp.268–87.
Couey, J.J. et al., 2013. Recurrent inhibitory circuitry as a mechanism for grid formation. *Nature Neuroscience*, 16(3), pp.318–324.
DeFelipe, J. et al., 2013. New insights into the classification and nomenclature of cortical GABAergic interneurons. *Nature reviews. Neuroscience*, 14(3), pp.202–16.
Deleuze, C., Pazienti, A. & Bacci, A., 2014. Autaptic self-inhibition of cortical GABAergic neurons: Synaptic narcissism or useful introspection? *Current Opinion in Neurobiology*, 26, pp.64–71.
Doischer, D. et al., 2008. Postnatal differentiation of basket cells from slow to fast signaling devices. *The Journal of neuroscience : the official journal of the Society for Neuroscience*, 28(48), pp.12956–68.
Domnisoru, C., Kinkhabwala, A.A. & Tank, D.W., 2013. Membrane potential dynamics of grid cells. *Nature*, 495(7440), pp.199–204.
Donato, F. et al., 2015. Early- and Late-Born Parvalbumin Basket Cell Subpopulations Exhibiting Distinct Regulation and Roles in Learning. *Neuron*, 85(4), pp.770–786.
Dufour, A. et al., 2016. Development of Synaptic Boutons in Layer 4 of the Barrel Field of the Rat Somatosensory Cortex: A Quantitative Analysis. *Cerebral cortex (New York, N.Y. : 1991)*, 26(2), pp.838–54.
Dyson, S.E. & Jones, D.G., 1980. Quantitation of terminal parameters and their interrelationships in maturing central synapses: A perspective for experimental studies. *Brain Research*, 183(1), pp.43–59.
Freund, T.F. & Buzsáki, G., 1998. Interneurons of the hippocampus. *Hippocampus*, 6(4), pp.347–470.
Fuchs, E.C. et al., 2015. Local and Distant Input Controlling Excitation in Layer II of the Medial Entorhinal Cortex. *Neuron*, 89(1), pp.194–208.

Fyhn, M. et al., 2007. Hippocampal remapping and grid realignment in entorhinal cortex. *Nature*, 446(7132), pp.190–4.
Fyhn, M. et al., 2004. Spatial representation in the entorhinal cortex. *Science (New York, N.Y.)*, 305(5688), pp.1258–64.
Gabriele, M.L., Brunso-Bechtold, J.K. & Henkel, C.K., 2000. Plasticity in the Development of Afferent Patterns in the Inferior Colliculus of the Rat after Unilateral Cochlear Ablation. *J. Neurosci.*, 20(18), pp.6939–6949.
Germroth, P., Schwerdtfeger, W.K. & Buhl, E.H., 1989. GABAergic neurons in the entorhinal cortex project to the hippocampus. *Brain research*, 494(1), pp.187–92.
Giocomo, L.M. et al., 2007. Temporal frequency of subthreshold oscillations scales with entorhinal grid cell field spacing. *Science (New York, N.Y.)*, 315(5819), pp.1719–22.
Goldberg, E.M. et al., 2011. Rapid developmental maturation of neocortical FS cell intrinsic excitability. *Cerebral cortex (New York, N.Y. : 1991)*, 21(3), pp.666–82.
Gonzalez-Sulser, A. et al., 2014. GABAergic projections from the medial septum selectively inhibit interneurons in the medial entorhinal cortex. *The Journal of neuroscience : the official journal of the Society for Neuroscience*, 34(50), pp.16739–43.
Grateron, L. et al., 2003. Postnatal development of calcium-binding proteins immunoreactivity (parvalbumin, calbindin, calretinin) in the human entorhinal cortex. *Journal of Chemical Neuroanatomy*, 26(4), pp.311–316.
Hafting, T. et al., 2005. Microstructure of a spatial map in the entorhinal cortex. *Nature*, 436(7052), pp.801–806.
Hargreaves, E.L., 2005. Major Dissociation Between Medial and Lateral Entorhinal Input to Dorsal Hippocampus. *Science*, 308(5729), pp.1792–1794.
Howat, W.J. & Wilson, B.A., 2014. Tissue fixation and the effect of molecular fixatives on downstream staining procedures. *Methods (San Diego, Calif.)*, 70(1), pp.12–9.
Hu, H., Gan, J. & Jonas, P., 2014. Fast-spiking, parvalbumin+ GABAergic interneurons: From cellular design to microcircuit function. *Science*, 345(6196), pp.1255263–1255263.
Insausti, R., Herrero, M.T. & Witter, M.P., 1997. Entorhinal cortex of the rat: cytoarchitectonic subdivisions and the origin and distribution of cortical efferents. *Hippocampus*, 7(2), pp.146–83.
Jones, R.S. & Bühl, E.H., 1993. Basket-like interneurones in layer II of the entorhinal cortex exhibit a powerful NMDA-mediated synaptic excitation. *Neuroscience letters*, 149(1), pp.35–9.
Jones, R.S.G. & Bühl, E.H., 1993. Basket-like interneurones in layer II of the entorhinal cortex exhibit a powerful NMDA-mediated synaptic excitation. *Neuroscience Letters*, 149(1), pp.35–39.
Kawaguchi, Y., 1995. Physiological subgroups of nonpyramidal cells with specific morphological characteristics in layer II/III of rat frontal cortex. *J. Neurosci.*, 15(4), pp.2638–2655.
Klink, R. & Alonso, A., 1997. Morphological characteristics of layer II projection neurons in the rat medial entorhinal cortex. *Hippocampus*, 7(5), pp.571–83.
Kraus, B.J. et al., 2015. During Running in Place, Grid Cells Integrate Elapsed Time and Distance Run. *Neuron*, 88(3), pp.578–589.
Kropff, E. et al., 2015. Speed cells in the medial entorhinal cortex. *Nature*, 523(7561), pp.419–24.
Langston, R.F. et al., 2010. Development of the Spatial Representation System in the Rat. *Science*, 328(5985), pp.1576–1580.
Lever, C. et al., 2009. Boundary vector cells in the subiculum of the hippocampal formation. *The Journal of neuroscience : the official journal of the Society for Neuroscience*,

29(31), pp.9771–7.
Li, Z. et al., 2004. The importance of dendritic mitochondria in the morphogenesis and plasticity of spines and synapses. *Cell*, 119(6), pp.873–87.
Van der Loos, H. & Glaser, E.M., 1972. Autapses in neocortex cerebri: synapses between a pyramidal cell's axon and its own dendrites. *Brain research*, 48, pp.355–60.
Mauceri, D. et al., 2015. Nuclear Calcium Buffering Capacity Shapes Neuronal Architecture. *The Journal of biological chemistry*, 290(38), pp.23039–49.
Meyer, A.H. et al., 2002. In vivo labeling of parvalbumin-positive interneurons and analysis of electrical coupling in identified neurons. *The Journal of neuroscience : the official journal of the Society for Neuroscience*, 22(16), pp.7055–64.
Miettinen, M. et al., 1996. Coexistence of parvalbumin and GABA in nonpyramidal neurons of the rat entorhinal cortex. *Brain research*, 706(1), pp.113–22..
Mittmann, W., Koch, U. & Häusser, M., 2005. Feed-forward inhibition shapes the spike output of cerebellar Purkinje cells. *The Journal of physiology*, 563(Pt 2), pp.369–78.
Morris, R. et al., 1982. Place navigation impaired in rats with hippocampal lesions. *Nature*, 297(5868), pp.681–683.
Moser, E.I. et al., 2014. Grid cells and cortical representation. *Nature Reviews Neuroscience*, 15(7), pp.466–481.
Mozhayeva, M.G. et al., 2002. Development of vesicle pools during maturation of hippocampal synapses. *The Journal of neuroscience : the official journal of the Society for Neuroscience*, 22(3), pp.654–65.
Nitsch, R., Soriano, E. & Frotscher, M., 1990. The parvalbumin-containing nonpyramidal neurons in the rat hippocampus. *Anatomy and Embryology*, 181(5), pp.413–425.
Novikoff, A.B. et al., 1972. Diffusion artificats in 3,3'-diaminobenzidine cytochemistry. *The journal of histochemistry and cytochemistry : official journal of the Histochemistry Society*, 20(9), pp.745–9.
O'Keefe, J., 1976. Place units in the hippocampus of the freely moving rat. *Experimental Neurology*, 51(1), pp.78–109. Available at:
O'Keefe, J. & Dostrovsky, J., 1971. The hippocampus as a spatial map. Preliminary evidence from unit activity in the freely-moving rat. *Brain Research*, 34(1), pp.171–175.
Packer, A.M. & Yuste, R., 2011. Dense, unspecific connectivity of neocortical parvalbumin-positive interneurons: a canonical microcircuit for inhibition? *The Journal of neuroscience : the official journal of the Society for Neuroscience*, 31(37), pp.13260–71.
Park, E., Dvorak, D. & Fenton, A.A., 2011. Ensemble place codes in hippocampus: CA1, CA3, and dentate gyrus place cells have multiple place fields in large environments. *PloS one*, 6(7), p.e22349.
Pastoll, H., Ramsden, H.L. & Nolan, M.F., 2012. Intrinsic electrophysiological properties of entorhinal cortex stellate cells and their contribution to grid cell firing fields. *Frontiers in neural circuits*, 6, p.17.
Petralia, R.S. et al., 2013. Sonic hedgehog promotes autophagy in hippocampal neurons. *Biology open*, 2(5), pp.499–504.
Ray, S. & Brecht, M., 2016. Structural development and dorsoventral maturation of the medial entorhinal cortex. *eLife*, 5, p.e13343.
Rockland K. *Axons and brain architechture*, pp, 356. Adacemic press, London.
Sanes, D.H. & Takács, C., 1993. Activity-dependent refinement of inhibitory connections. *The European journal of neuroscience*, 5(6), pp.570–4.
Sargolini, F. et al., 2006. Conjunctive representation of position, direction, and velocity in entorhinal cortex. *Science (New York, N.Y.)*, 312(5774), pp.758–62.
Savelli, F., Yoganarasimha, D. & Knierim, J.J., 2008. Influence of boundary removal on the

spatial representations of the medial entorhinal cortex. *Hippocampus*, 18(12), pp.1270–82.
Schmidt-Hieber, C. & Häusser, M., 2013. Cellular mechanisms of spatial navigation in the medial entorhinal cortex. *Nature neuroscience*, 16(3), pp.325–31.
Seil, F.J. & Drake-Baumann, R., 1994. Reduced cortical inhibitory synaptogenesis in organotypic cerebellar cultures developing in the absence of neuronal activity. *The Journal of comparative neurology*, 342(3), pp.366–77.
Seress, L. & Ribak, C., 1990. Postnatal development of the light and electron microscopic features of basket cells in the hippocampal dentate gyrus of the rat. *Anatomy and Embryology*, 181(6), pp.547–65.
Seress, L. & Ribak, C.E., 1990. The synaptic connections of basket cell axons in the developing rat hippocampal formation. *Experimental brain research*, 81(3), pp.500–8.
Shen, D.-N. et al., 2015. Autophagy in synaptic development, function, and pathology. *Neuroscience bulletin*, 31(4), pp.416–26.
Sik, A. et al., 1995. Hippocampal CA1 interneurons: an in vivo intracellular labeling study. *The Journal of neuroscience : the official journal of the Society for Neuroscience*, 15(10), pp.6651–65.
Solstad, T. et al., 2008. Representation of geometric borders in the entorhinal cortex. *Science (New York, N.Y.)*, 322(5909), pp.1865–8.
Somogyi, P., 1977. A specific "axo-axonal" interneuron in the visual cortex of the rat. *Brain research*, 136(2), pp.345–50.
Soriano, E. et al., 1993. Chandelier cells in the hippocampal formation of the rat: the entorhinal area and subicular complex. *The Journal of comparative neurology*, 337(1), pp.151–67.
Stensola, H. et al., 2012. The entorhinal grid map is discretized. *Nature*, 492(7427), pp.72–8.
Strange, B.A. et al., 2014. Functional organization of the hippocampal longitudinal axis. *Nature Reviews Neuroscience*, 15(10), pp.655–669.
van Strien, N.M., Cappaert, N.L.M. & Witter, M.P., 2009. The anatomy of memory: an interactive overview of the parahippocampal-hippocampal network. *Nature reviews. Neuroscience*, 10(4), pp.272–82.
Tamás, G., Buhl, E.H. & Somogyi, P., 1997. Massive autaptic self-innervation of GABAergic neurons in cat visual cortex. *The Journal of neuroscience : the official journal of the Society for Neuroscience*, 17(16), pp.6352–64.
Tang, G. et al., 2014. Loss of mTOR-dependent macroautophagy causes autistic-like synaptic pruning deficits. *Neuron*, 83(5), pp.1131–43.
Tang, Q. et al., 2014. Pyramidal and stellate cell specificity of grid and border representations in layer 2 of medial entorhinal cortex. *Neuron*, 84(6), pp.1191–7.
Taube, J.S., Muller, R.U. & Ranck, J.B., 1990. Head-direction cells recorded from the postsubiculum in freely moving rats. I. Description and quantitative analysis. *Journal of Neuroscience*, 10(2), pp.420–435.
Tyzio, R. et al., 1999. The establishment of GABAergic and glutamatergic synapses on CA1 pyramidal neurons is sequential and correlates with the development of the apical dendrite. *The Journal of neuroscience : the official journal of the Society for Neuroscience*, 19(23), pp.10372–82.
Varga, C., Lee, S.Y. & Soltesz, I., 2010. Target-selective GABAergic control of entorhinal cortex output. *Nature neuroscience*, 13(7), pp.822–4.
Vida, I., Bartos, M. & Jonas, P., 2006. Shunting inhibition improves robustness of gamma oscillations in hippocampal interneuron networks by homogenizing firing rates. *Neuron*, 49(1), pp.107–17.

Wills, T.J. et al., 2010. Development of the hippocampal cognitive map in preweanling rats. *Science (New York, N.Y.)*, 328(5985), pp.1573–6.
Wills, T.J., Muessig, L. & Cacucci, F., 2014. The development of spatial behaviour and the hippocampal neural representation of space. *Philosophical transactions of the Royal Society of London. Series B, Biological sciences*, 369(1635), p.20130409.
Witter, M.P. et al., 1989. Functional organization of the extrinsic and intrinsic circuitry of the parahippocampal region. *Progress in Neurobiology*, 33(3), pp.161–253.
Witter, M.P. & Amaral, D., 2004. Hippocampal formation. In G. Paxinos, ed. *The rat nervous system*. Elsevier academic press, pp. 637–687.
Wittmann, M. et al., 2009. Synaptic activity induces dramatic changes in the geometry of the cell nucleus: interplay between nuclear structure, histone H3 phosphorylation, and nuclear calcium signaling. *The Journal of neuroscience : the official journal of the Society for Neuroscience*, 29(47), pp.14687–700.
Wouterlood, F.G. et al., 1995. Parvalbumin-immunoreactive neurons in the entorhinal cortex of the rat: localization, morphology, connectivity and ultrastructure. *Journal of Neurocytology*, 24(2), pp.135–153.
Wouterlood, F.G. & Pothuizen, H., 2000. Sparse colocalization of somatostatin- and GABA-immunoreactivity in the entorhinal cortex of the rat. *Hippocampus*, 10(1), pp.77–86.
Yekhlef, L. et al., 2015. Selective activation of parvalbumin- or somatostatin-expressing interneurons triggers epileptic seizurelike activity in mouse medial entorhinal cortex. *Journal of neurophysiology*, 113(5), pp.1616–30.
Yushkevich, P et al., 2006. Users-guided 3D active contour segmentation of anatomical structures: Significantly improved effeciency and reliability. *Neuroimage*, 31(3), pp.1116-28.

Appendix I: Images from immunohistochemical testing

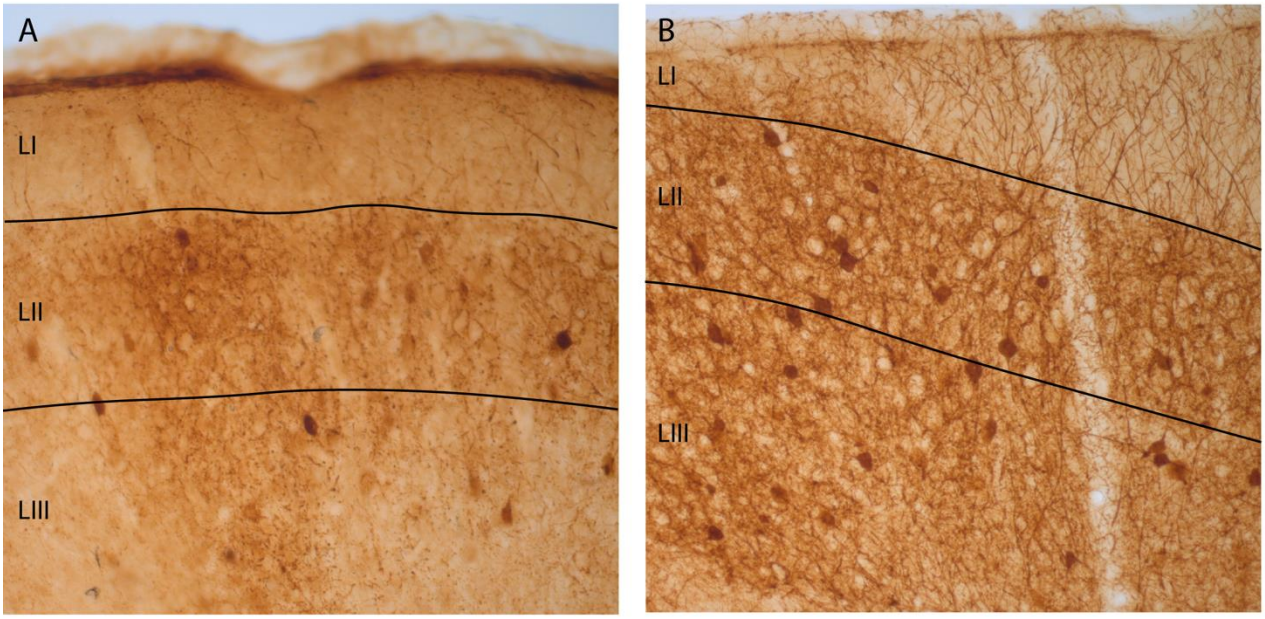

Figure 11: Light micrographs illustrating PV expression within the MEC with different immunohistochemical protocols. (A) With the original protocol, cell bodies and dendritic arborization were poorly defined (P90). (B) After adapting the new protocol, all cellular compartments can be visualized (P30). Cortical layers are indicated with roman numbers. Images captured with x20 objectives.

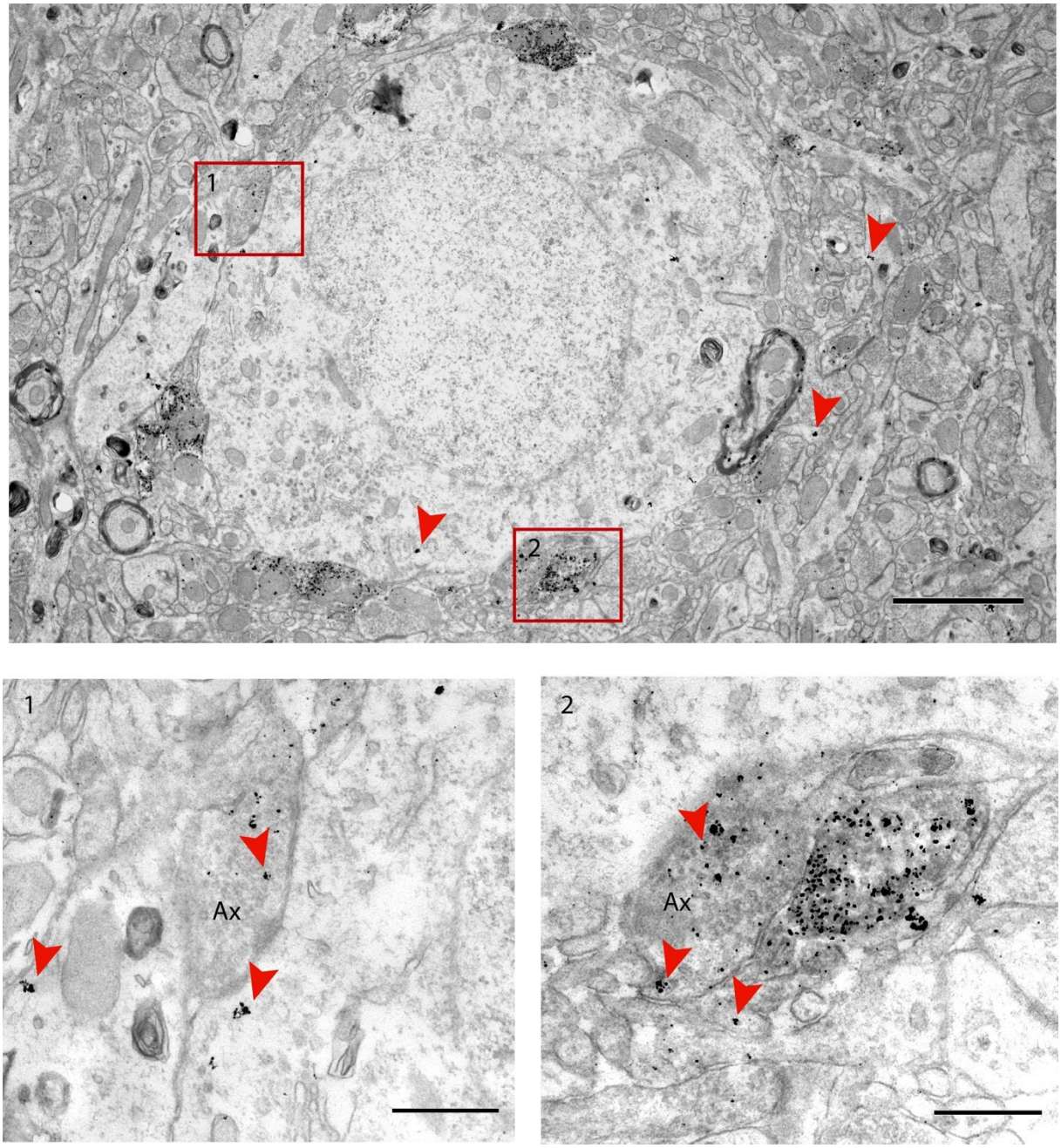

Figure 12: Electron micrograph illustrating background staining (arrows) on a immunonegative axon terminal (Ax) and somata resulting from the original EM protocol. Scale bar 2µm and 500nm (box 1 and 2).

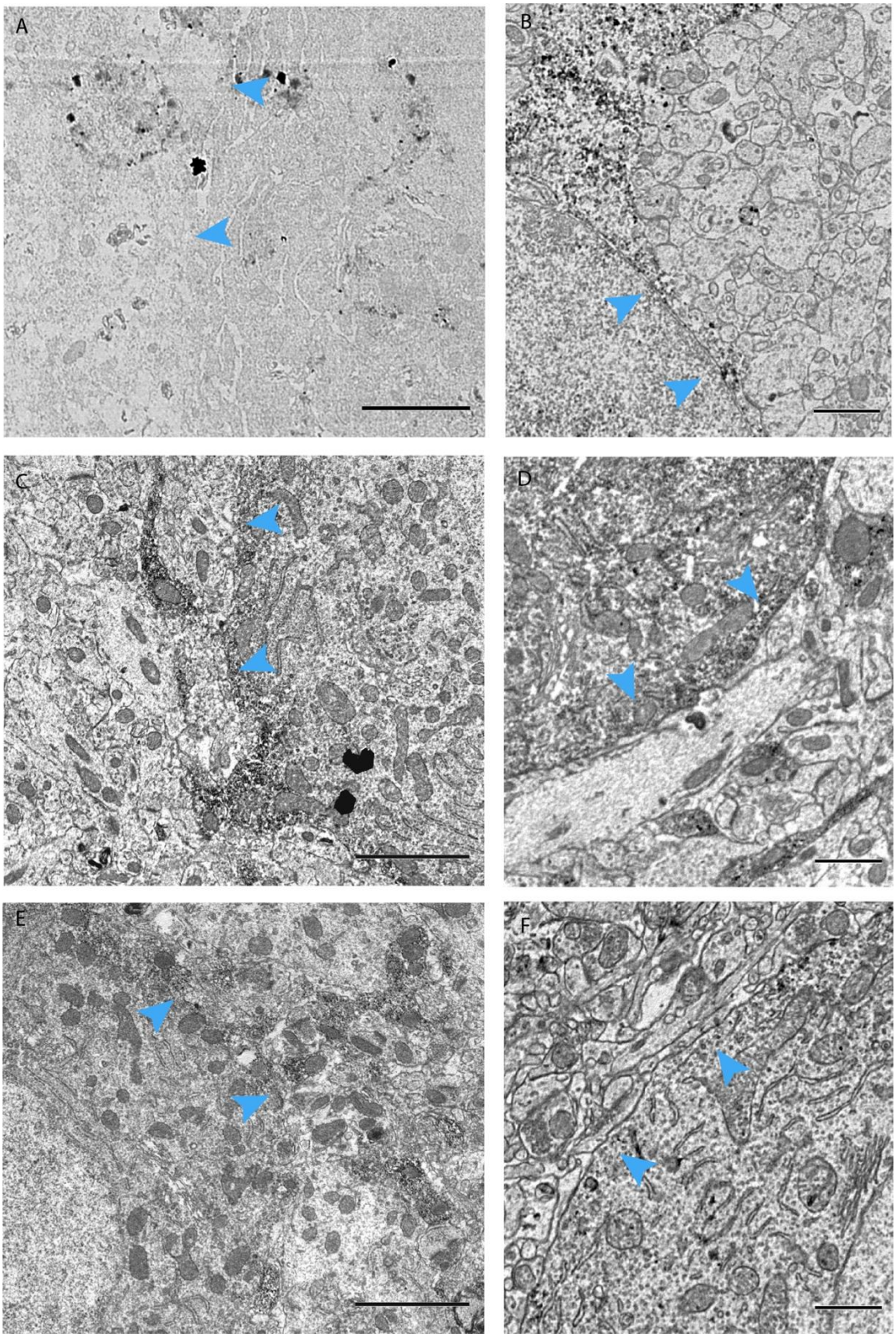

Figure 13: Electron micrographs illustrating differences in membrane visibility with two different immunohistochemical protocols. Poorly defined membranes (arrows) resulting from the adaption of the immunohistochemical protocol from the Kavli Institute for (A) P10, (C) P15 and (E) P30. The final immunohistochemical protocol for EM resulted in sufficiently defined membranes for (B) P10, (D) P15 and (F) P30. Scale bar 2µm.

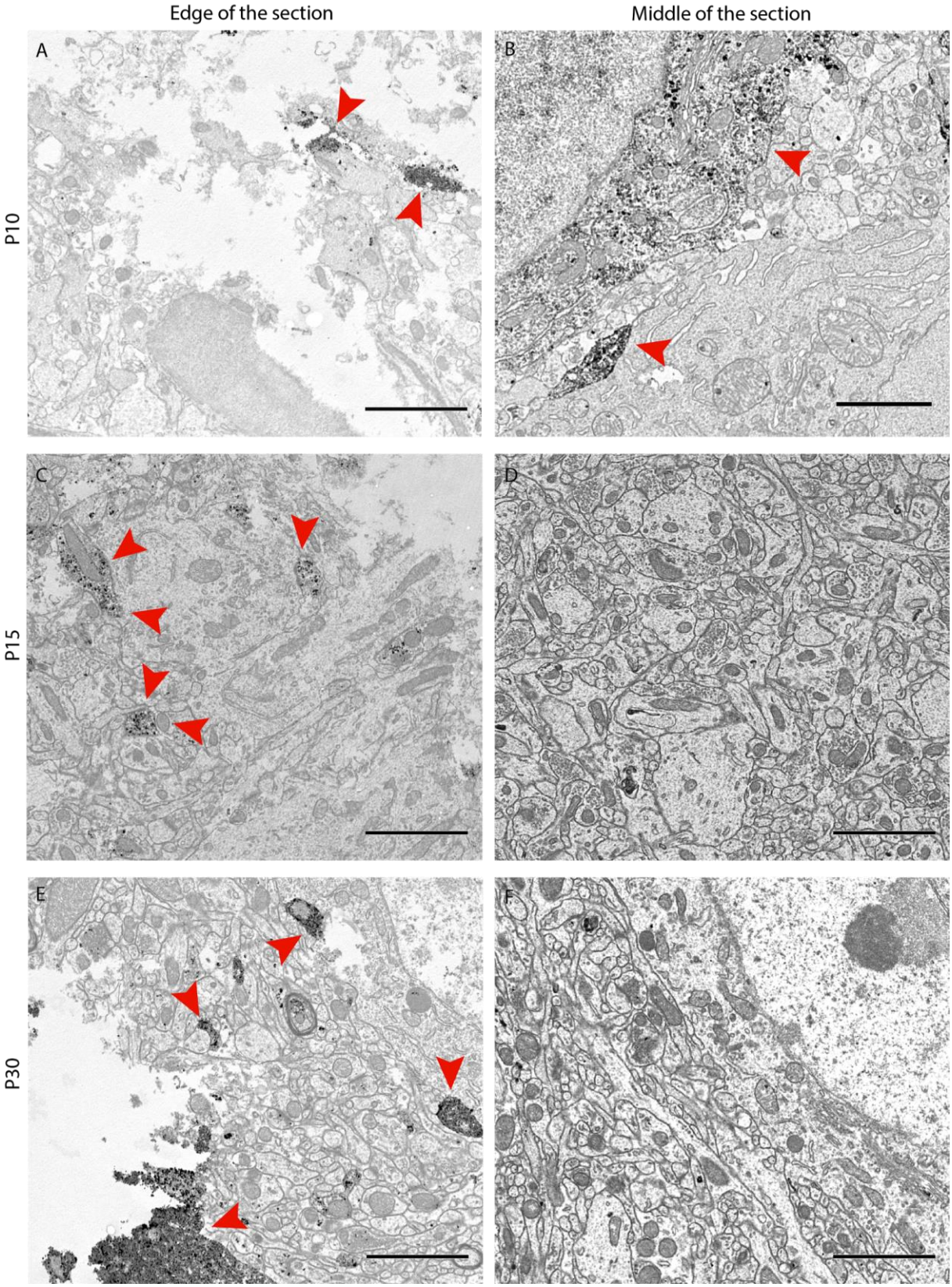

Figure 14: Electron micrographs illustrating the result of a single step TX-100. All animals displayed good morphology. The labeling in (A) P10 were specific and distributed within the whole section, while the labeling in (B) P15 and (C) P30 were sparse and restricted to the edges of the sections. Arrows indicate PVG-labeling. Scale bar 2µm.

Appendix II: Protocols

See appendix III for recipes of all solutions used in the following protocols. The pH of the solutions is 7.4-7.5, the molarities of the buffers is 0.1, solutions are diluted in MilliQ water and the sections are placed on a shaker unless otherwise specified.

A. Original fluorescence protocol from the Kavli Institute

1. 3 x 15 minutes in 0.125M PB
2. 2 x 10 minutes in 0.125M PB + 1% Tx-100
3. 60 minutes in 5% normal horse serum + 0.125M PB + 1% Tx-100
4. Incubate with primary antibody diluted to 1:1000 in 0.125M PB + 1% Tx-100 + 5% normal horse serum for 24 hours at 4°C
5. 4 x 15 minutes in 0.125M PB
6. Incubate with secondary antibody diluted to 1:400 in 0.125M PB + 1% Tx-100 for 24 hours at 4°C
7. 4 x 15 minutes in 0.125M PB

B. Immunohistochemical protocol for LM adapted from the Kavli Institute with modifications

1. 3 x 15 minutes in PB
2. 2 x 10 minutes in PB + 1% Tx-100
3. 30 minutes in 1% H_2O_2 in 50% MeOH + PB
4. 3 x 15 minutes in PB
5. 60 minutes in PB + 1% Tx-100 + 5% normal horse serum
6. Incubate with primary antibody diluted to 1:40 000 in PB + 1% Tx-100 + 5% normal horse serum overnight at 4°C
7. 4 x 15 minutes in PB
8. Incubate with secondary antibody diluted to 1:400 in PB + 1% Tx-100 overnight at 4°C
9. 4 x 15 minutes in PB
10. 60 minutes in ABC reagent + PB
11. 4 x 15 minutes in PB
12. Stain with 0.05% DAB + 0.01% H_2O_2 for 8 minutes in the dark
13. 3 x 15 minutes in PB
14. 2 x 10 minutes in MilliQ water
15. Air dry and mount with mounting medium

C. Final immunohistochemical protocol for LM

1. PB 3 x 15 minutes
2. 2 x 10 minutes in PB + 1% Tx-100
3. 30 minutes in 1% H_2O_2 in 50% MeOH in PB
4. 3 x 15 minutes in PB
5. 60 minutes in PB + 1% Tx-100 + 5% normal horse serum
6. Incubate with primary antibody diluted to 1:40 000 in PB + 1% Tx-100 + 5% normal horse serum overnight at 4°C

7. 4 x 15 minutes in PB
8. Incubate with secondary antibody diluted to 1:200 in PB + 1% Tx-100 overnight at 4°C
9. 4 x 15 minutes in PB
10. 60 minutes in ABC reagent + PB
11. Stain with 0.05% DAB + 0.01% H_2O_2 for 8 minutes in the dark
12. 3 x 10 minutes in PB
13. 2 x 10 minutes in MilliQ water
14. Air dry and mount with mounting medium

D. Original immunohistochemical protocol for EM

1. 3 x 10 minutes in TBS
2. 2 x 15 minutes in 0.1% sodium borohydride + TBS
3. 3 x 10 minutes in TBS
4. 30 minutes in TBS + 0.05% Tx-100
5. 2 x 5 minutes in TBS
6. 30 minutes in 1% H_2O_2 in 50% MeOH + TBS
7. 3 x 10 minutes in TBS
8. Block with incubation medium containing 10% normal horse serum for 2 hours
9. Incubate with primary antibody, diluted to 1:20 000 with incubation medium with 1% normal horse serum, overnight at 4°C
10. 3 x 10 minutes with TBS + 0.05% Tx-100
11. Incubate with secondary antibody, diluted to 1:200 with incubation medium, for 2 hours
12. 3 x 10 minutes in TBS + 0.05% Tx-100
13. 1 hour with ABC reagent + TBS
14. 3 x 10 minutes in TBS + 0.05% Tx-100
15. Stain with 0.05% DAB + 1% H_2O_2 for 4 minutes in the dark
16. 3 x 10 minutes in TBS
17. 3 x 10 minutes in Sørensens PB
18. Fix in 2.5% glutaraldehyde + Sørensens PB for 1 hour
19. 3 x 10 minutes in Sørensens PB
20. Inspect sections for labeling in LM

    Use acid washed glassware and boiled MilliQ water from this point, and transfer sections into a sterile well.
21. 3 x 10 minutes in 2% SoAc (pH 8.7)
22. 4% Sodium thioglycolate at 4°C overnight
23. 3 x 10 minutes in 2% SoAc (pH 8.7)
24. Silver development solutions for 8 minutes in the dark
25. 2 minutes in 1% acetic acid
26. 3 x 10 minutes with 2% SoAc (pH 8.7)
27. 0.05% gold chloride ($AuCl_3$) for 15 minutes in the dark
28. 3 x 10 minutes with 2% SoAc (pH 8.7)
29. 10 minutes in 3% Sodium thiosulphate
30. 3 x 10 minutes in 2% SoAc (pH 8.7)

    See protocol F for post-fixation

E. Final immunohistochemical protocol for EM

1. 5 x 7 minutes in PB
2. 20 minutes in PB + 0.05% Tx-100
3. 5 x 7 minutes in PB
4. 30 minutes in 1% H_2O_2 + 5+% MeOH + PB
5. 5 x 7 minutes in PB
6. 90 minutes in 1% BSA + 1% normal horse serum + PB + 0.05% Triton X-100
7. Incubate with primary antibody, diluted to 1:40 000 in PB + 1% BSA + 1% normal horse serum, overnight at 4°C
8. 5 x 7 minutes in PB
9. Incubate with secondary antibody diluted to 1:400 in PB for 2 hours
10. 5 x 7 minutes in PB
11. 60 minutes in ABC reagent + PB
12. 5 x 7 minutes in PB
13. Stain with 0.03% DAB + 1% H_2O_2 for 5 minutes (P15 & P30) or 8 (P10) minutes in the dark
14. 5 x 7 minutes in PB
15. Inspect sections for labeling in LM

    Use acid washed glassware and boiled MilliQ water from this point, and transfer sections into a sterile well.
16. 3 x 10 minutes in 2% SoAc (pH 8.7)
17. 4% Sodium thioglycolate at 4°C overnight
18. 3 x 10 minutes in 2% SoAc (pH 8.7)
19. Silver development solutions for 8 minutes in the dark
20. 3 x 10 minutes in 2% SoAc (pH 8.7)
21. 0.05% gold chloride ($AuCl_3$) for 15 minutes in the dark
22. 3 x 10 minutes in 2% SoAc (pH 8.7)
23. 10 minutes in 3% Sodium thiosulphate
24. 3 x 10 minutes in 2% SoAc (pH 8.7)
    See protocol F for post-fixation

F. Post-fixation

1. 2 x 10 minutes in cacodylate buffer
   Transfer samples to dram glass
2. 15 minutes in 1% OsO_4 + 1.5% $K_4Fe(CN)_6$ in the dark
3. Wash 2 x 15 minutes in cacodylate buffer
4. Dehydrate in 50 – 70 – 90% ethanol, each 10 minutes
5. 4 x 15 minutes 100% ethanol
6. 2 x 15 minutes in acetone
7. Infiltrate with increased concentration of epoxy resin (added 0.15ml DMP30) in acetone: 2+1 x 2 hours, 1+1 x 2 hours, 1 + 2 overnight on a rotator
8. 6 + 2 hours in fresh epoxy resin on rotator
9. Flat embed overnight: put sections between two sheets of Aclar film and then between two microscope slides. Polymerize at 60°C for 1 day

10. Mount on epoxy block: glue the selected are on flat epoxy resin blocks with fresh epoxy resin. Polymerize for 3-4 days at 60°C

G. Contrastain with uranyl acetate and lead citrate

4% uranyl acetate in 50% etanol
1% lead citrate in sodium hydroxide (NaOH)

1. Place grid (with section facing down) on drop of uranyl acetate for 8 minutes in the dark
2. Rinse in 8 x 10 seconds in fresh sterile water.
3. Dry grid with lens paper
4. Place grid (with section facing down) on drop of lead citrate for 3-4 minutes in the dark
5. Rinse in 8 x 10 seconds in fresh sterile water.
6. Dry grid with lens paper

Appendix III: Recipes for solutions

DAB (0.03%) stock solution
0.15g DAB
5ml MilliQ water

1. Dissolve the DAB in MilliQ water
2. Add concentrated HCl drop by drop under vigorous stirring, until the solution is no longer white

Epoxy resin (320g)
153.4 g LX-112 Epoxy resin
81.1g DDSA
65.5g 1,4-Dihydro-Cinnamylidenemalonic acid (NMA)
Mix under vigorous stirring

Incubation medium (50ml: pH 7.4)
1% BSA (2273 µl from stock 22%)
0.1% glycine (0.05g)
0.1% lysine monohydrochloride (0.05g)
0.1% cold water fish gelatin (125µl from stock 40%)
0.05% Triton X-100 (2500µl from stock 1%)
1% normal horse serum
5000µl 1M stock solution
Fill up with sterile water

PB 0.4M stock solution (pH 7.4)
Solution A: Mono sodium phosphate ($NaH_2PO_4H_2O$): 27.6g/500ml (M_w: 119,97g/mol)
Solution B: Dibasic dehydrate, base: ($Na_2HPO_4H_2O$): 36.5g/500ml (M_w: 141.95g/mol)

1. Make 500ml stock solution A
2. Make 500ml stock solution B
3. Add solution A to 500ml solution B until the pH is 7.4

Silver development solution
Stock solutions:

Solution A, 30 mL: new solution
1.5 g Na2CO3 (5% Sodium carbonate)
30 mL boiled MP water

Solution B, 50 mL: new solution
50 mL MP water
0.1 g Silver nitrate
0.1 g Ammonium nitrate (99%)
0.5 g Tungstosilicic acid

Dissolve first silver nitrate in boiled water. Next, add ammonium nitrate and Silico wolfram acid.

Solution C:
40 µl 37% formaldehyde (contains 10-15% methanol)

Working solution (5ml):

1. Add 10µl of solution C to 2.5ml of solution B under vigorous stirring
2. Add drop by drop of solution C+B to 2.5ml of solution A under vigorous stirring

Solution should remain clear and transparent, and is stable for 30 minutes only

Sørensens phosphate buffer 0.3M stock solution (500ml; pH 7.4)
19,23g di-Natriumhydrogenphosphate-Dihydrate (Na2HPO4 ×2H2O)
5,79g Natriumhydrogenphosphate Monohydrate (NaH2PO4 ×H2O)
3,68g NaCl
Add 500ml MilliQ water under vigorous stirring

TBS 1M stock solution (pH 7.4)
1M = 121g trizma base (Tris) (121.14g/mol)
0.9% = 90g NaCl
1. Add 400 ml sterile water
2. Adjust to pH 7.4 with 32% HCl or 1M HCl
3. Make volume up to 1l with MilliQ water

Appendix IV: List of antibodies and chemicals

Antibody	**Company**	**Product number**
Polyclonal goat anti-PV	Swant	PV-214
Biotiylanated anti-goat IgG in horse	Vector Laboratories	BA-9500

Chemicals	**Company**	**Product number**
1,4-Dihydro-Cinnamylidenemalonic acid (NMA)	Chemi-Teknik	20800
3,3'-Diaminobenzidine (DAB)	Sigma	32750
Acetic acid	Merck	100063
Acetone	VWR chemicals	20063.365
Ammonium nitrate	Sigma	A9642
Avidin-biotin complex (ABC)	Vector laboratories	BA2001
Bovine serum albumin 22%	Sigma	1001927547
Cold water fish gelatin	Sigma	G7041
di-Natriumhydrogenphosphate-Dihydrate	Merck	1.06580.1000
DDSA	Chemi-Teknik	21850
Dibasic dehydrate base	Sigma-Aldrich	101531765
DMP-30	Chemi-teknikk AS	21370
Etanol	Kemetyl Norge AS	
Formaldehyde	Sigma	F1635
Glutaraldehyde	Chemi-teknikk	16310
Glycine	Sigma	808822
Gold chloride ($AuCl_3$)	Merck	1582
H_2O_2	Sigma	31642
Hydrochloric acid	Sigma-Aldrich	258148
Lead citrate	Chemi-Teknik	17800
LX112 Epoxy resin	Chemi-Teknik	21650
Lycine monohydrochloride	Sigma	L-5626
Methanol	Sigma-Aldrich	101309083
Monos odiumphosphate	Sigma-Aldrich	101526916
Natriumhydrogenphosphate	Merck	1.06346.1000
Normal horse serum	Sigma	H0146
Osmiumtetroxide (OsO_4)	Chemi-Teknik	19110
Paraformaldehyde	Merck	1.04005.1000
Phosphate buffer saline (PBS)	Oxoid	BR0014G
Porcine skin gelatin	Sigma	1000722767
Potassium ferrocyanide ($K_4Fe(CN)_6$)	Sigma	P3289
Silver nitrate	Merck	1.01512.0025
Sodium acetate	Sigma	S8750
Sodium cacodylate trihydrate	Sigma-Aldrich	101537318
Sodium carbonate	Merck	6392
Sodium chloride (NaCl)	Merck	1.06404.1000
Sodium thioglycolate	Sigma	T0632
Sodium thiosulphate ($Na_2S_2O_3(3H_2O)$)	Sigma	72049
Tissue Mount (mounting medium)	Sakura	SAK1467
Toluidine Blue	Merck	1.15930.0025

Trisma baze	Merck	1.08382.0500
Triton X-100	Chemi-Teknik AS	22140
Tungstosilicic acid	Merck	10659
Uranyl acetate	Chemi-Teknik	22400